Final Research Report

Project Title: **Boron-Based Hydrogen Storage: Ternary Borides and Beyond**

Award Number: DE-EE0006630

Project Period: August 1, 2014 to January 31, 2016

Report submission date: April 28, 2016

Recipient:
HRL Laboratories, LLC
3011 Malibu Canyon Road
Malibu, California 90265

Working Partners:
HRL Laboratories
Sandia National Laboratories
University of Missouri, St. Louis

Cost-Sharing Partners: HRL Laboratories

Principal Investigator:
John J. Vajo
Senior Scientist
Phone: 310-317-5745
Email: jjvajo@hrl.com

Submitted by:
Richard Warren
Contracts Manager
Phone: 310-317-5590
Email: HRLLabsContracts@hrl.com

DOE Project Manager:
Katie Randolph
(720) 356-1759
Katie.Randolph@go.doe.gov

Executive Summary: DOE continues to seek reversible solid-state hydrogen materials with hydrogen densities of ≥11 wt% and ≥80 g/L that can deliver hydrogen and be recharged at moderate temperatures (≤100 °C) and pressures (≤100 bar) enabling incorporation into hydrogen storage systems suitable for transportation applications. Boron-based hydrogen storage materials have the potential to meet the density requirements given boron's low atomic weight, high chemical valance, and versatile chemistry. However, the rates of hydrogen exchange in boron-based compounds are thus far much too slow for practical applications. Although contributing to the high hydrogen densities, the high valance of boron also leads to slow rates of hydrogen exchange due to extensive boron-boron atom rearrangements during hydrogen cycling. This rearrangement often leads to multiple solid phases occurring over hydrogen release and recharge cycles. These phases must nucleate and react with each other across solid-solid phase boundaries leading to energy barriers that slow the rates of hydrogen exchange.

This project sought to overcome the slow rates of hydrogen exchange in boron-based hydrogen storage materials by minimizing the number of solid phases and the boron atom rearrangement over a hydrogen release and recharge cycle. Two novel approaches were explored: 1) developing matched pairs of ternary borides and mixed-metal borohydrides that could exchange hydrogen with only one hydrogenated phase (the mixed-metal borohydride) and only one dehydrogenated phase (the ternary boride); and 2) developing boranes that could release hydrogen by being lithiated using lithium hydride with no boron-boron atom rearrangement.

For the first approach, possible pairs of ternary borides and mixed-metal borohydrides based on Mg with various first row transition metals were investigated both experimentally and theoretically. In particular, the Mg/Mn ternary boride and mixed-metal borohydride were found to be a suitable pair and synthesized using novel synthetic approaches. Dehydrogenation of the Mg/Mn mixed metal borohydride with a capacity of ~8 wt% was shown to begin at 150 °C, which is ~100 °C lower than the temperature for pure magnesium borohydride. However, the borohydride did not appear to reform upon hydrogenation. Similarly, significantly more hydrogen uptake was demonstrated in the Mg/Mn ternary boride compared to pure magnesium boride, although the absolute hydrogen uptake was small, only ~1 wt%.

For the second approach, a variety of different borane substrates were evaluated experimentally for lithiation with lithium hydride. These included molecular boranes, polymeric boranes, and Li/B alloys, which represented the dehydrogenated state of the lithiation reaction. Polymeric boranes showed evidence for reversible hydrogen storage based on the lithiation reaction with lithium hydride. However, dehydrogenation capacity was low, < 1 wt%, with poor reversibility. Computational studies were performed to evaluate the thermodynamics of the lithiation reaction for a series of molecular boranes. This evaluation proved difficult because the calculations had to include both 1) the molecular nature of the borane and 2) the solid phases of the borane and lithium hydride. The enthalpy of dehydrogenation was estimated to be ±25 kJ/mol-H_2 for extended borane structures, B_nH_x, with n>20. Thus, the dehydrogenation reaction may be exothermic accounting for the poor reversibility measured experimentally.

Overall, based on the initial consideration given in this project, it does not appear that ternary borides or lithiation of boranes will readily yield hydrogen storage materials that can meet the DOE targets.

1. Project Goal and Objectives: The overall goal of this project is to develop boron-based hydrogen storage materials with gravimetric hydrogen capacities of >11 wt% with thermodynamic and kinetic properties required for vehicle applications.

The objectives of this project are to experimentally and theoretically discover and evaluate 1) novel ternary borides and mixed metal borohydrides that store and release hydrogen while maintaining single hydrogenated and dehydrogenated phases and 2) a new class of materials termed "lithiated boranes" that store and release hydrogen by exchanging boron-hydrogen bonds in molecular boranes, or related materials such as nanoparticle or polymeric boranes, with boron-lithium bonds from lithium hydride while preserving the underlying boron-boron bond framework.

The expected outcomes are 1) synthesis and characterization of novel ternary borides and an evaluation of their ability to store hydrogen by hydrogenating to mixed metal borohydrides, 2) identification of boranes or related materials that store hydrogen via lithiation reactions, and 3) an initial assessment of these materials to reversibly store hydrogen.

2. Background: Boron is an attractive element for material-based hydrogen storage. In particular, metal borohydrides have been identified by the DOE Metal Hydride Center of Excellence as prospective truly remarkable hydrogen storage materials, given their potentially large storage capacities and the wide variety of properties observed. Boron's light-weight and high chemical valence enable high gravimetric hydrogen storage densities, versatile chemistry, and potentially adjustable storage thermodynamics. However, a persistent challenge with reversible boron-based hydrogen storage is that the kinetics (the reaction rates) of hydrogen exchange are typically too slow for practical applications, even if thermodynamics might be nearly optimal. While there are several experimentally demonstrated and/or theoretically predicted reversible boron-based hydrogen storage systems with attractive thermodynamics, none of them have acceptable kinetics.

The kinetic barriers originate from the chemical bond transformations that occur during hydrogen exchange. Bonding in boron compounds is often covalent or ionic, both of which are directional. Thus, the energetic barriers associated with off-directional intermediate states in the chemical transformations of boron are high. It is likely that these high barriers slow atom diffusion and therefore the rates of hydrogen exchange. In addition, the high chemical valency of boron results in reactions with large boron atom rearrangements. For example, reversible hydrogen storage in borohydrides span stoichiometries from fully hydrogenated $[BH_4]^-$ anions with isolated boron atoms surrounded by and bound only to hydrogen to dehydrogenated networks of boron atoms bound mainly to each other. Such large changes result in multiple solid phases requiring diffusion of directionally bonded atoms. This gives rise to additional energetic barriers associated with nucleation of new phases and interfaces between phases. These barriers contribute to the slow kinetics of current boron-based hydrogen storage materials.

The slow kinetics of covalently bound systems have been improved by using scaffolds to reduce particle sizes to the nanometer scale and thereby limit diffusion lengths. Significant increases in hydrogen exchange rates have been demonstrated, although this approach is limited because the energy barriers for individual diffusion events, the extent of atomic rearrangement, and interfacial energies between phases are all largely unchanged. There are also ~25% gravimetric

and volumetric storage density penalties associated with using even the best possible scaffolds. To achieve the hydrogen exchange rates needed for practical applications, and to eliminate the storage density penalties, further improvements are needed.

While reducing diffusion lengths, nanoscale approaches to improving kinetics do not address the intrinsic limitations of high diffusion and interfacial energy barriers. These intrinsic limitations may be addressed by developing systems with minimal, preferably single, hydrogenated and dehydrogenated phases. For boron-based materials, ternary borides $M_aM_bB_x$ that reversibly hydrogenate to single phase mixed-metal borohydrides $M_aM_b(BH_4)_x$ via the reaction

$$M_aM_bB_x + 2xH_2 \leftrightarrow M_aM_b(BH_4)_x$$

satisfy this criteria, with the choice of metals enabling high hydrogen capacities (~ 11 wt% H_2) and tuning to optimize the thermodynamics and potentially act catalytically.

This project is focused on developing this class of materials by experimentally and computationally exploring ternary borides and mixed metal borohydrides based on Mg with the first row transition metals V, Cr, Mn, Fe, and Co. Mg forms a hexagonal binary boride (MgB_2, P_6/mmm). The transition metals V, Cr, Mn, Fe, and Co also form hexagonal borides isostructural with MgB_2 (Figure 1). This suggests that hexagonal single-phase ternary borides of these transition metals with Mg may be expected. In addition, the varying Pauling electronegativities (Table 1) enable tuning of the stability using the established inverse relationship, i.e., increasing average electronegativity decreases borohydride stability. Thus, using M_a = Mg and M_b = V, Cr, Mn, Fe or Co, gives five new hydrogen storage reaction systems that all have gravimetric hydrogen storage densities >11 wt% (Table 1).

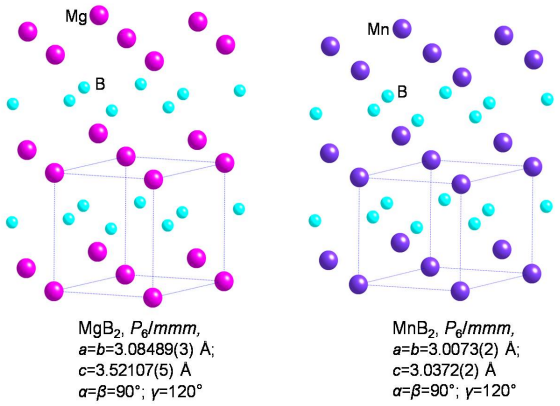

Figure 1. Crystal structures of isomorphous MgB_2 and MnB_2. The similarity suggests the feasibility of ternary boride phase formation.

Metal	Mg	Mn	V	Cr	Fe	Co
χ_P	1.31	1.55	1.63	1.66	1.83	1.88
wt%H, $M_aM_b(BH_4)_x$	14.9	11.6	12.0	11.9	11.6	11.3

Table 1. Metal electronegativity (χ_P) and borohydride gravimetric hydrogen density for Mg and selected transition metals (M_b) with potential to form ternary borides. Stability would decrease from Mn to Co.

In a second approach, we hypothesize that the kinetic barriers associated with B-B bond breaking can be eliminated by molecular B_nH_x or extended borane networks $(BH_x)_n$, that store hydrogen by reversibly reacting with LiH to form "lithiated boranes" ($B_nH_{x-y}Li_y$) via the reaction

$$B_nH_x + yLiH \leftrightarrow B_nH_{x-y}Li_y + yH_2$$

in which B-H bonds are replaced by B-Li bonds from LiH and releasing H_2 while preserving the underlying boron framework. This reaction would constitute a new class of high-capacity reversible hydrogen storage materials. Retaining the boron framework without needing to break and reform any B-B bonds could lead to greatly improved kinetics, although there are still two phases, with an interface (B_nH_x/LiH), that must react during dehydrogenation. A stable B-B framework could also eliminate the production of B_2H_6, promoting release of pure H_2 without volatilization of the hydrogen storage medium.

This project is also focused on developing this new class of reversible hydrogen storage materials by experimentally surveying a variety of molecular and extended borane substrates together with computations on the energetics of lithium substituted boranes. Boron's chemical versatility includes a rich variety of boron hydrides (boranes) that could participate in such reactions. Molecular boranes (B_nH_x) with up to n ~ 20 are known with the larger species based on fragments or linked fragments of an icosahedron boron cluster (Figure 2). Compounds with n >~ 10, have x ~ n, give stoichiometries with hydrogen capacities of ~10 wt%. A hypothetical example in which only the terminal B-H bonds of decaborane are lithiated is

$$B_{10}H_{14} + 10LiH \leftrightarrow B_{10}Li_{10}H_4 + 10H_2$$

which could store 9.8 wt% hydrogen. The energetics of lithiated borane compounds are, however, unknown and will be studied computationally. Larger *conjuncto*-boranes in which two or more smaller boranes are linked by B-B bonds are also known. This enables a very large number of polymeric boranes with extended boron frameworks. Depending on the symmetry of the linkages, networks in the form of approximately 2D extended sheets all the way to 3D porous structures should be possible. A wide variety of borane-based anions, carboboranes, and partially substituted boranes are also known. In terms of the size and extent of the boron framework, the substrate classes considered included 1) discrete molecular boranes (n<~50); 2) nanoparticle boranes (n ~ 50 to 1000); 3) extended framework nanoporous boranes (n unlimited); and 4) in the dehydrogenated state, macroscopic B/Li alloys (n unlimited).

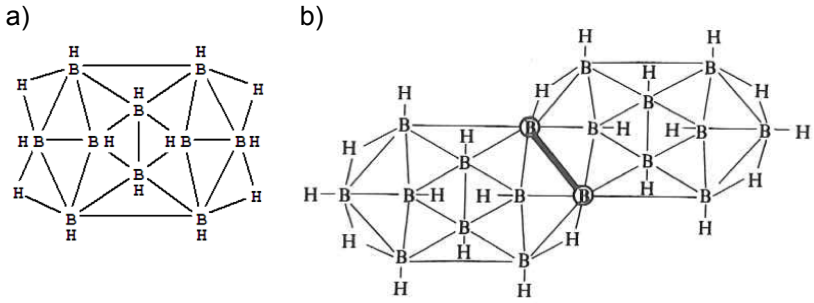

Figure 2. Plane projection structures of a) $B_{10}H_{14}$ (decaborane) and b) $B_{18}H_{22}$ showing possible substrates for hydrogen storage via lithiation with LiH. Thick B-B bond indicates union of two (initially) B_{10} fragments.

Prototypical molecular substrates include decaborane ($B_{10}H_{14}$) and the associated carboborane ($C_2B_{10}H_{12}$). These are shown schematically in Figure 3. Decaborane has a open cage, cup-like, boron framework with 10 terminal B-H and 4 bridging B-H-B bonds. In contrast, carboborane contains two C atoms in the framework that completes the cage with 12 terminal B-H or C-H bonds. Isomers with the C atoms in *ortho* (Figure 3) and *meta* positions are known.

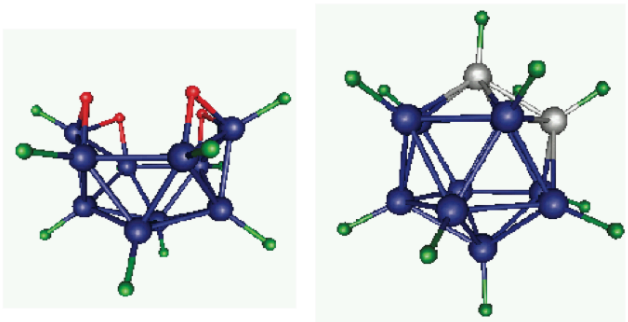

$B_{10}H_{14}$ **o-$C_2B_{10}H_{12}$**

Figure 3. Molecular structures for $B_{10}H_{14}$ and o-$C_2B_{10}H_{12}$. Atom colors: boron (blue); terminal hydrogen (green); bridging hydrogen (red); carbon (gray).

Decaborane was studied (1) as a substrate with LiH for the synthesis of $Li_2B_{12}H_{12}$ according to the reaction

$$1.2B_{10}H_{14} + 2LiH \rightarrow Li_2B_{12}H_{12} + 3.4\ H_2$$

In this study *ex-situ* XRD was used to monitor the extent of reaction. After 15 hr at 200 °C, product peaks were observed, although no new peaks were seen after only 10 hr. The evolution of H_2 was apparently not monitored. Formation of $Li_2B_{12}H_{12}$ requires rearrangement of the boron framework in addition to reaction with LiH. Further reaction with additional LiH up to a stoichiometry of $B_{10}H_{14}$ + 10LiH might occur and could be tracked by monitoring H_2 evolution. To avoid boron framework rearrangement and salt formation, an analogous reaction with carboborane ($C_2B_{10}H_{14}$ + 12LiH) could be tried. Electronic modification of the boron framework is also possible by substituting a B-H with electron donating or withdrawing groups. In general, the substitutional chemistry of boranes is well developed.

In the small molecule limit, single boron atom substituted ammonia boranes may be considered as substrates. Ammonia borane reacts with LiH to form the lithium ammonia borane $LiNH_2$-

BH_3. This reaction involves a relatively acidic N-H hydrogen and thus is exothermic and not reversible. If further reaction is possible with either the N-H or the B-H hydrogen atoms, reversibility may be possible. To isolate any reaction to the B-H bonds, a fully substituted species on the N atom, such as $(CH_3)_3N\text{-}BH_3$ could be studied.

Larger, nanoparticle boranes may be more amenable to Li exchange without unwanted side reactions. Elemental nanoparticle boron has been studied although hydrogenated nanoparticle boranes appear less well known. Recently, nanoparticles with the composition $BH_{0.36}$ have been synthesized by high energy mechanical milling in Professor Scott Anderson's group at the University of Utah (2). These nanoparticles were also studied with DFT calculations. Examples from the computations and the synthesis are shown in Figure 4.

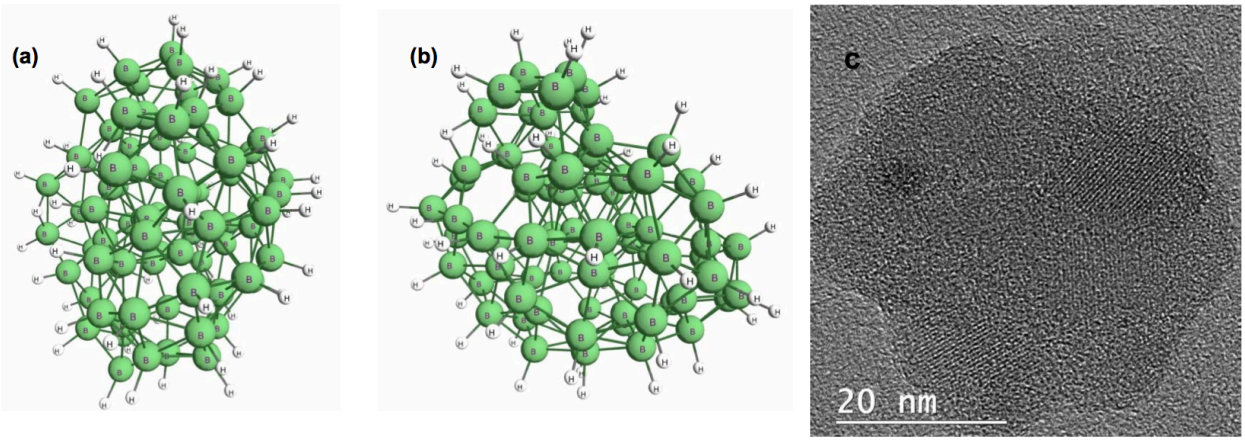

Figure 4. Simulated and synthesized hydrogenated borane nanoparticles from U. Utah (2). The B-H bonds are thought to be predominately on the particle surfaces.

Highly porous boranes, boron with B-H surface terminations, could be an ideal substrate for Li/H exchange if they could be formed and if LiH could be infiltrated into the pore volume. Such materials could be monolithic or granular on a macroscale while still retaining porous nanoscale internal structure. Porous borane substrates could be formed by templating, using a zeolite or porous silica as a scaffold. Decaborane, which melts at ~100 °C, could be melt infiltrated into the scaffold. This precursor could then be polymerized by moderate controlled pyrolysis followed by removal of the template. The pyrolysis conditions could be determined on bulk samples using thermogravimetric analysis (TGA). Removing the template without also degrading, oxidizing, the borane may be difficult. One possibility is deaerated and cold concentrated HF.

Deintercalation may be another synthetic route to achieving porous boranes by extracting the metal component for a metal boride leaving the boron atom framework. This chemistry has not been applied to borides; however, an analogous reaction was reported for silicides (3). In that work cold HCl at -30 °C was used to remove Ca from $CaSi_2$ without oxidizing the Si according to the reaction

$$3CaSi_2 + 7HCl \rightarrow Si_6H_6 \bullet HCl + 3CaCl_2$$

The Si_6H_6 product was in the form of 2-dimensional sheets as shown in Figure 5.

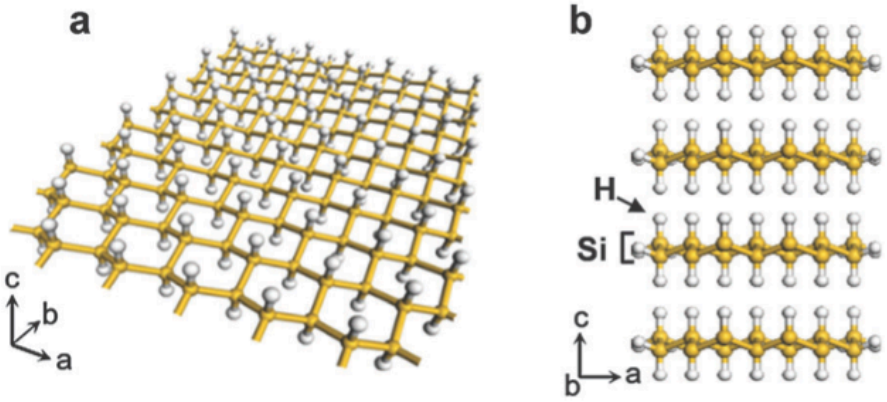

Figure 5. Schematic of (a) silicon nanosheet and (b) layered polysilane (Si_6H_6). From (3).

Interestingly, this Si_6H_6 material was reacted with Li metal, by mechanical milling to release H_2 as shown by the scheme in Figure 6. This reaction is similar to the B_nH_x/LiH exchange reaction being explored in this project except that the substrate is Si instead of B and the exchange was conducted with Li metal instead of LiH. Actually, it would be interesting to try exchanging Si_6H_6 with LiH or to try hydrogenating the Si_6Li_6 product.

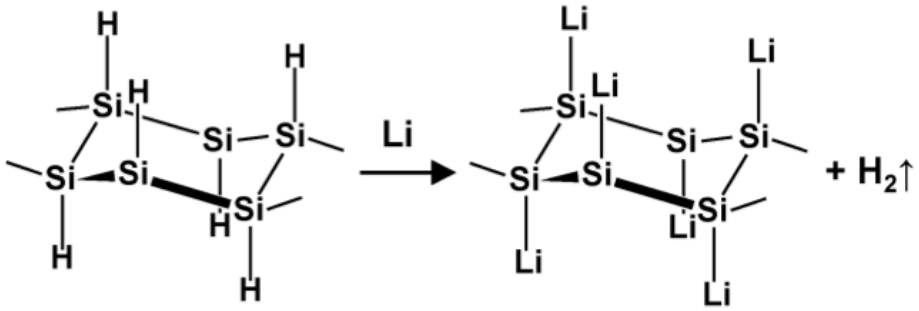

Figure 6. Proposed reaction for formation of Si_6Li_6 by mechanical milling with Li metal.(4)

It is not known whether similar chemistry is possible with metal borides. If such reactions are possible MgB_2, which contains hexagonal layers of boron interspersed with layers of Mg (as shown in Figure 1) could yield BH in the form of 2-dimensional sheets according to the reaction

$$MgB_2 + 2HCl \rightarrow 2BH + MgCl_2$$

These sheets may serve as good substrates for H/Li exchange with LiH.

A fully Li exchanged borane would be a type of lithium boride and constitute the dehydrogenated phase of the hydrogen storage reaction. Therefore, another class of substrates could be bulk B-Li phases. The B-Li binary phase diagram, shown in Figure 7 contains several phases. The phase near 50 atomic percent B, with an exact composition of B_6Li_7 has been synthesized and characterized (5). The synthesis was performed from a mixture of B + Li, sealed under Ar in steel ampoules and heated at 450 °C for 48 hr. As shown in the inset to Figure 7, the structure contains linear chains of B atoms surrounded by Li. This phase could hydrogenate to a BH_x + LiH mixture. Hydrogenation of B_6Li_7 has been investigated (6, 7) However, these studies were focused on full hydrogenation to $LiBH_4$ where the linear B chains in the B_6Li_7 alloy were completely separated into individual BH_4^- anions. Formation of $LiBH_4$ required heating to 700

°C, although approximately one equivalent of hydrogen was absorbed at much lower temperature, ~225 °C. The form of this hydrogen or its reversibility was not characterized.

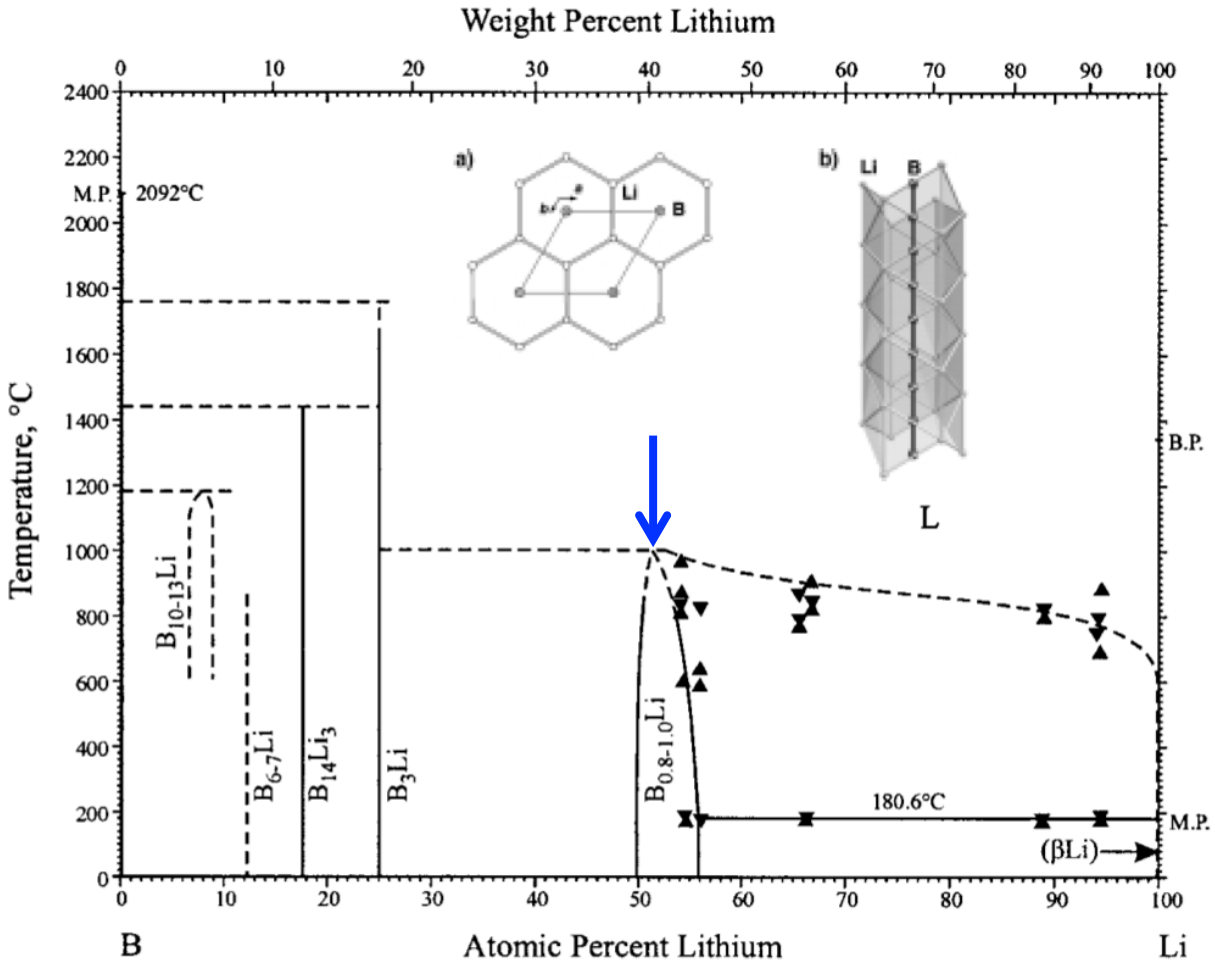

Figure 7. Boron-lithium phase diagram. The B_6Li_7 phase is marked (blue arrow). Insets show a top-down projection along the c-axis (a) and a 3-dimensional view (b) of the B_6Li_7 structure.

3. Accomplishment — synthesis and hydrogen cycling of Mg/Mn ternary metal borides: Preparation methods for ternary metal borides can be classified into several groups: 1) direct reaction of the elements; 2) borothermic reduction; 3) carbothermic reduction; 4) electrochemical reduction in molten salt electrolytes; and 5) molecular precursor decomposition, such as the borohydride dehydrogenation being explored in this project. These methods were all being considered together with a new method involving a direct alloying reaction of MgB_2 with a transition metal or a transition metal boride.

3.1 Synthesis of nanophase MgB_2: Initially, phase pure MgB_2 was synthesized by reaction of (excess) elemental Mg and B at 680 °C in a seal stainless steel container. The XRD pattern of the as-synthesized product is shown in Figure 8 (blue curve). The SEM image (Figure 8, right) of the product reveals large agglomerates of several micrometers in size. Ball-milling MgB_2 using high-energy SPEX milling yields a material, which still displays d-spacing values characteristic to P_6/mmm MgB_2 Figure 8 (red curve). However, the XRD peaks display significant peak broadening Figure 8 (purple curve), which indicates the presence of small grains. The SEM images confirm the particle size is significantly reduced upon ball-milling to about 20-80 nm. A Rietveld refinement of the XRD pattern of the ball-milled MgB_2 powder reveals a crystallite size of about 21 nm. The results are promising, as small particles are known to display higher reactivity and conversion in solid-state reactions.

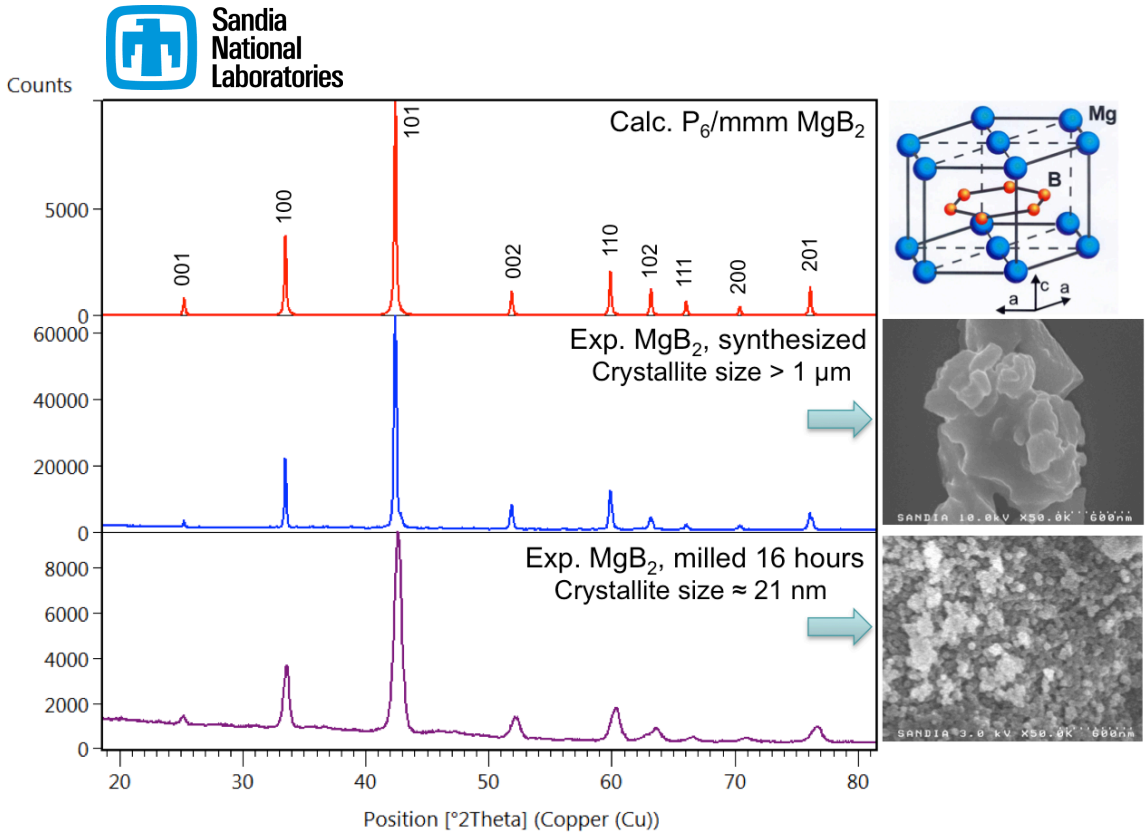

Figure 8. XRD patterns (left) and the corresponding SEM images (right) of as-synthesized and ball-milled MgB_2. The calculated MgB_2 pattern, P_6/mmm space group and the crystal structure are shown as well (top).

3.2 Synthesis of Mg/Mn ternary metal borides: Using the synthesized MgB_2, forming a ternary boride via a direct alloying reaction was tested. Commercial MnB_2 was used with the borides milled together in a 1:1 molar ratio. Milling was conducted in a SPEX 8000 mill for 16 hr with hardened steel balls at room temperature. The results are shown in Figure 9. The commercial MnB_2 contains Mn_3B_4 as an impurity phase, although the symmetry of the diboride component can still be recognized as identical to MgB_2. After milling, the diffraction peaks are broadened, as expected. In addition, the symmetry is retained indicating a single phase. Importantly, the peaks are intermediate in diffraction angle between those of MgB_2 and MnB_2. This is most easily seen for the intense 101 peaks at ~ 45 degrees two-theta. This suggests formation of a $Mg_{0.5}Mn_{0.5}B_2$ ternary boride. To characterize the distribution of Mg and Mn in the product

phase, energy dispersive x-ray spectroscopy (EDS) was performed. The results are shown in Figure 10. The SEM image indicates that the product is composed of highly agglomerated sub-micrometer particles. At the resolution of the analysis, ~ 100 nm, the Mg and Mn appear well mixed. Further characterization is still required to confirm the structure and composition of this phase. Nevertheless, the apparent stability of this ternary boride with respect to the binary borides is a necessary and important step toward realizing a mixed borohydride/ternary boride hydrogen storage material.

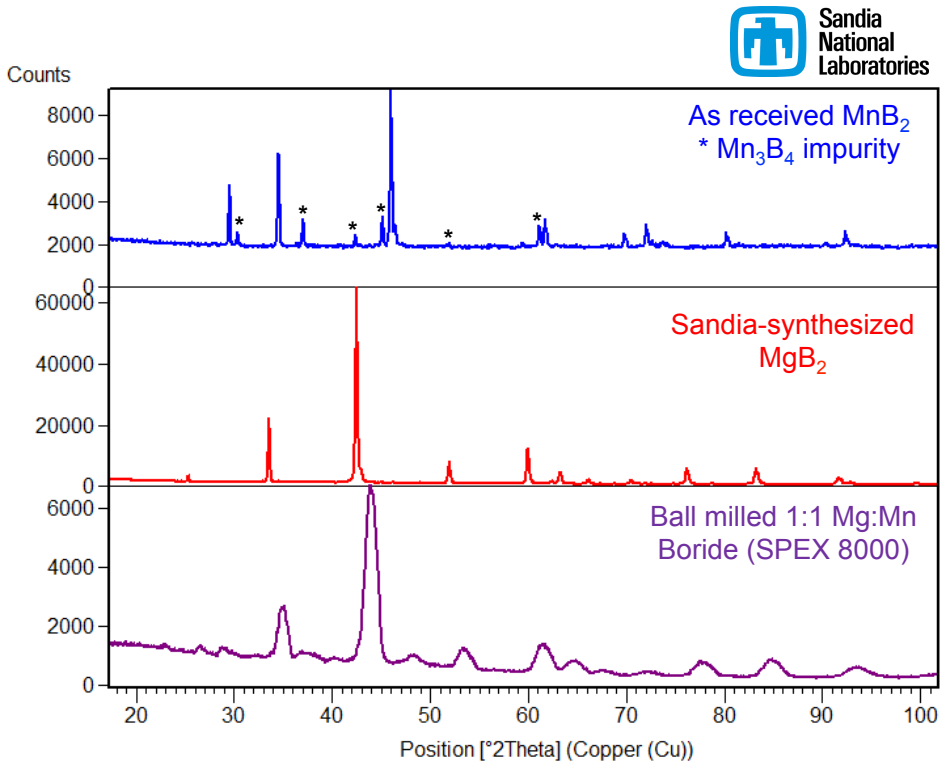

Figure 9. XRD patterns for commercial MnB_2, synthesized MgB_2, and alloying reaction product after high energy milling in a 1:1 molar ratio.

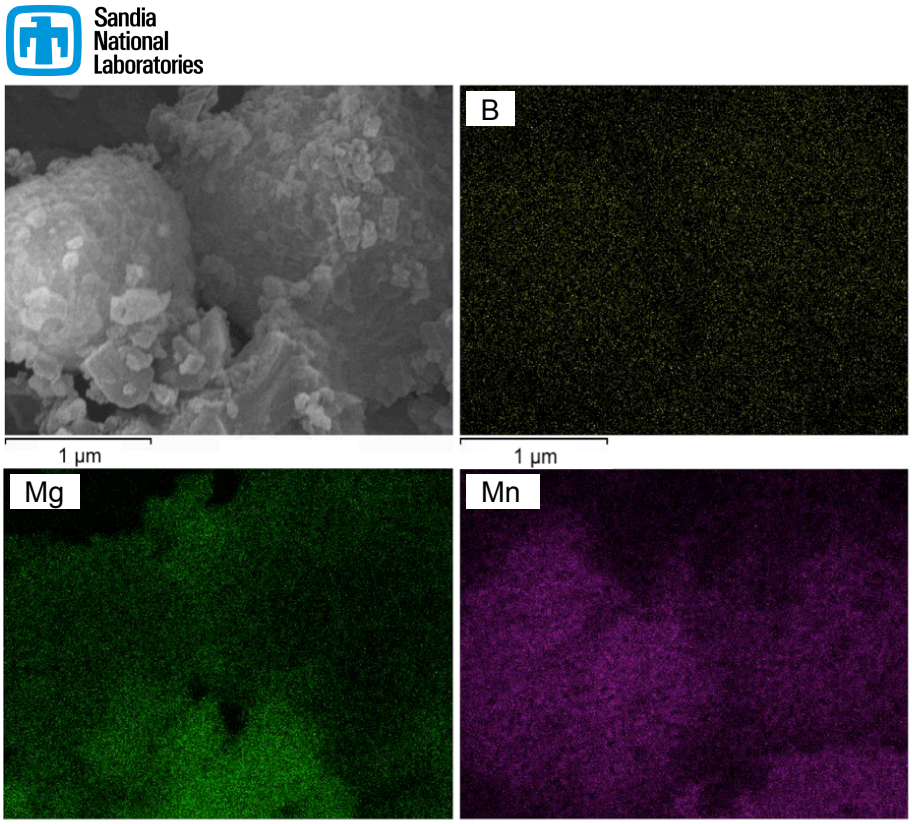

Figure 10. SEM and EDX maps for B, Mg, and Mn in the milled MgB_2 + MnB_2 reaction product.

In addition to $Mg_{0.5}Mn_{0.5}B_2$ ternary borides with the compositions of $Mg_{0.75}Mn_{0.25}B_2$ and $Mg_{0.9}Mn_{0.1}B_2$ were synthesized. The $Mg_{0.75}Mn_{0.25}B_2$ ternary boride were predicted to be unstable with respect to $Mg_{0.66}Mn_{0.33}B_2$ and pure MgB_2. Therefore, to check the stability of $Mg_{0.75}Mn_{0.25}B_2$ and $Mg_{0.9}Mn_{0.1}B_2$ synthesized by milling, which could yield metastable solid solutions, samples were annealed at 500 °C for 72 hr and characterized by XRD. The results are shown in Figure 11. After annealing, the peak widths sharpen, as expected, but they also shift to slightly lower 2theta angles closer to pure MgB_2. Traces of peaks for MnB_2 also appear, eg at 46 degrees 2-theta, although these peaks are not as apparent as the peaks for MgB_2. The change is much less apparent for the $Mg_{0.9}Mn_{0.1}B_2$ sample suggesting that this composition might be stable or at least closer to a stable solid solution.

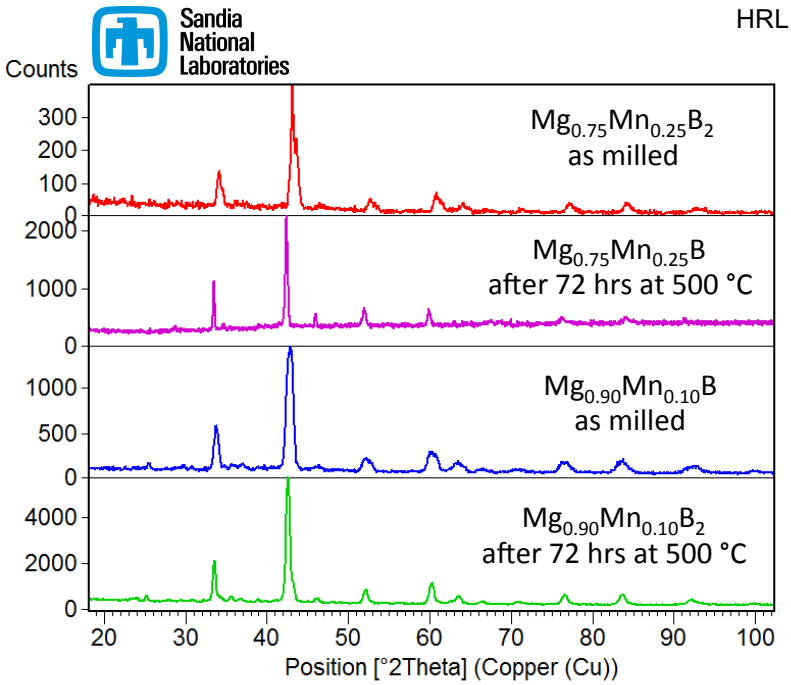

Figure 11. XRD patterns of Mg/Mn ternary borides as milled and after annealing at 500 °C for 72 hr.

3.3 Hydrogen cycling of Mg/Mn ternary metal borides: The hydrogen cycling behavior of $Mg_{0.75}Mn_{0.25}B_2$ was investigated. A sample was hydrogenated in 150 bar of H_2 for 38 hr at 380 °C. After 38 hr, the uptake was estimated to be ~1.2 wt%. Thus, the hydrogenation kinetics for this sample are still slow. Dehydrogenation, shown in Figure 12, began at ~225 °C and with heating to 400 °C, ~0.8 wt% H_2 was desorbed indicating significant reversibility.

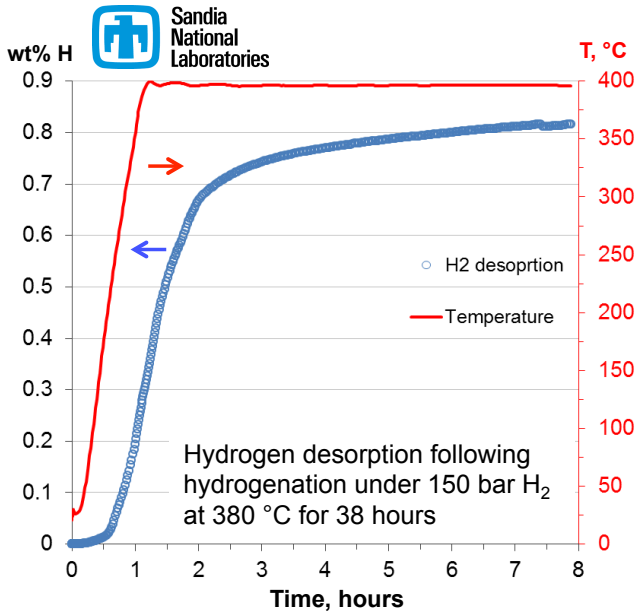

Figure 12. Dehydrogenation of $Mg_{0.75}Mn_{0.25}B_2$ after hydrogenation at 150 bar H_2, 380 °C for 38 hr.

Hydrogenation of $Mg_{0.75}Mn_{0.25}B_2$ was also studied at HRL. Several hydrogenations (labeled H1, H2, and H3) and dehydrogenation treatments (labeled D1 and D2) were performed. The hydrogenations were performed at ~160 bar, 380 °C for 2 to 6 hr and the estimated uptake was 0.5 wt%. The treatment order was H1, H2, D1, H3, and D2. The dehydrogenations D1 and D2 are shown in Figure 13a. Hydrogen desorption begins at ~250 °C in agreement with the data from Sandia in Figure 12. FTIR following hydrogenation H3 is shown in Figure 13b. The three-band fingerprint from $[BH_4]^-$ is seen together with additional B-H bonding.

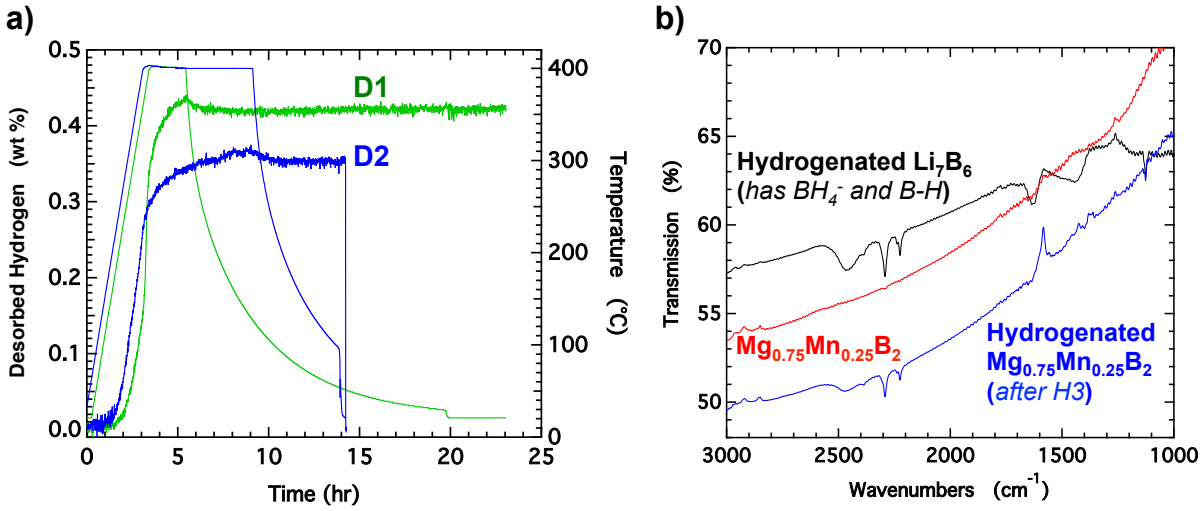

Figure 13. Dehydrogenation and FTIR spectra of $Mg_{0.75}Mn_{0.25}B_2$. a) dehydrogenations D1 and D2 after, respectively, hydrogenations H2 (160 bar H_2, 380 °C for 6 hr) and H3 (160 bar H_2, 300 °C, 350 °C, and 380 °C each for 2 hr). b) FTIR spectra after hydrogenation H3 compared to as milled sample and hydrogenated Li_7B_6.

3.4 Comparison of ternary boride and binary boride hydrogenation: Hydrogenation of a sample of $Mg_{0.75}Mn_{0.25}B_2$ sent to HRL showed the three-band fingerprint characteristic of $[BH_4]^-$ (Figure 13b) Samples of milled MgB_2 and MnB_2 were also hydrogenated to compare to the ternary boride. A comparison of the FTIR spectra B-H stretching region after attempting to hydrogenate the MgB_2 sample is shown in Figure 14. After hydrogenation in 200 bar H_2 at temperatures varying from 250 °C to 325 °C a barely detectable absorption of the $[BH_4]^-$ fingerprint was seen. The absorption increased slightly after performing a subsequent hydrogenation at 350 °C. A subsequent dehydrogenation showed only traces of hydrogen, ~0.05 wt% (data not shown), together with the disappearance of the $[BH_4]^-$ fingerprint stretches. Interestingly, 200 bar and 350 °C is below the equilibrium pressure estimated in Ozolins *et al.*(8) In comparison, much more intense $[BH_4]^-$ stretches are observed after hydrogenation of the $Mg_{0.75}Mn_{0.25}B_2$ alloy. This comparison indicated that formation of the ternary boride dramatically improves the hydrogenation kinetics, possibly due to the catalytic effect of the Mn. However, overall, the extent of hydrogenation achieved is still small, ~1 wt% hydrogen. Although expected to be relatively unstable, similar hydrogenation was attempted on the milled MnB_2 sample; no $[BH_4]^-$ fingerprint stretching was observed (data not shown).

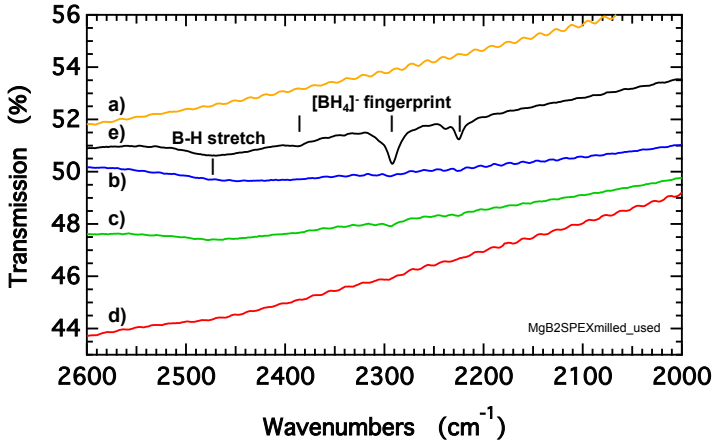

Figure 14. FTIR spectra of B-H stretch region for MgB_2 samples. a) after SPEX milling. b) after hydrogenation in 200 bar H_2 from 250 °C to 325 °C. c) after hydrogenation at 350 °C. d) after desorption at 400 °C. e) after hydrogenation of $Mg_{0.75}Mn_{0.25}B_2$.

4. Accomplishment — synthesis and hydrogen cycling of Mg/Mn borohydrides: To compare with to the hydrogenation of the ternary borides, achieving a single hydrogenated phase/single dehydrogenated phase hydrogen storage material was also investigated beginning with hydrogenated mixed metal borohydride phase. To synthesize a mixed-metal borohydride, a common synthesis scheme for the separate borohydrides was developed.

4.1 Syntheses of $Mg(BH_4)_2$ and $Mn(BH_4)_2$: Initial work began with a solution approach to synthesize pure $Mg(BH_4)_2$ borohydride by reacting dibutylmagnesium with excess borane-dimethylsulfide, BH_3-$S(CH_3)_2$, in a heptane/toluene solution. An adduct of magnesium borohydride, $Mg(BH_4)_2$-$(S(CH_3)_2)_2$, is formed initially. This adduct can be converted into α-$Mg(BH_4)_2$ by mild heating at 120 °C in vacuum. Results from an initial synthesis are shown using x-ray diffraction (XRD) in Figure 15. Compared to the adduct and a calculated XRD pattern, the isolated $Mg(BH_4)_2$ is free from the adduct and compares very well with the expected structure.

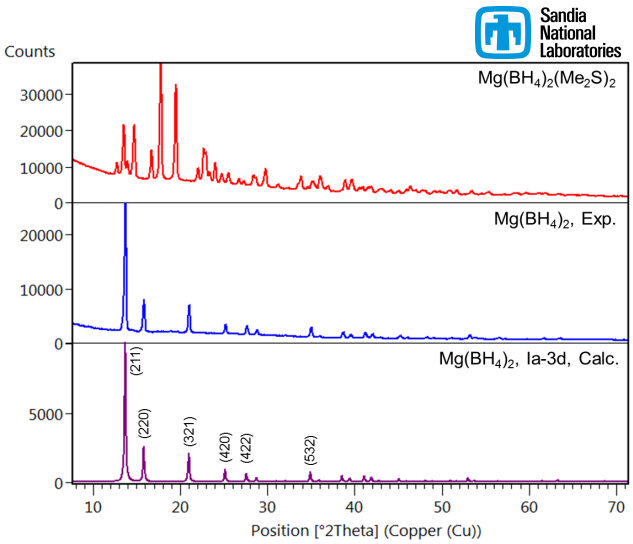

Figure 15. X-ray diffraction analysis of $Mg(BH_4)_2$ synthesis. Top (red) trace $Mg(BH_4)_2$-$(S(CH_3)_2)_2$ adduct; middle (blue) isolated $Mg(BH_4)_2$; bottom (purple) trace calculated pattern for $Mg(BH_4)_2$.

An analogous synthetic scheme was used to synthesize $Mn(BH_4)_2$. Unlike dibutylmagnesium, which is available commercially, the corresponding dibutylmanganese is not available and was synthesized following a literature recipe from $MnBr_2$ and a solution of n–butyllithium in hexane. The dimethylsulfide adduct formed initially was decomposed by heating under vacuum at 110 °C. The results from this new synthetic route for $Mn(BH_4)_2$ are shown in Figure 16. Compared to the adduct and the calculated XRD pattern, the isolated $Mn(BH_4)_2$ is free from the adduct and compares very well with the expected structure.

This material, together with the $Mg(BH_4)_2$ synthesized previously could be used to make Mg/Mn mixed-metal borohydrides by a solid state route using mechanical milling or a solution based route by co-dissolving $Mg(BH_4)_2$ and $Mn(BH_4)_2$ in a mutual solvent and trying to crystallize a mixed-metal product. Alternatively, the dimethylsulfide based scheme could be applied directly to a mixture of dibutylmagnesium and dibutylmanganese.

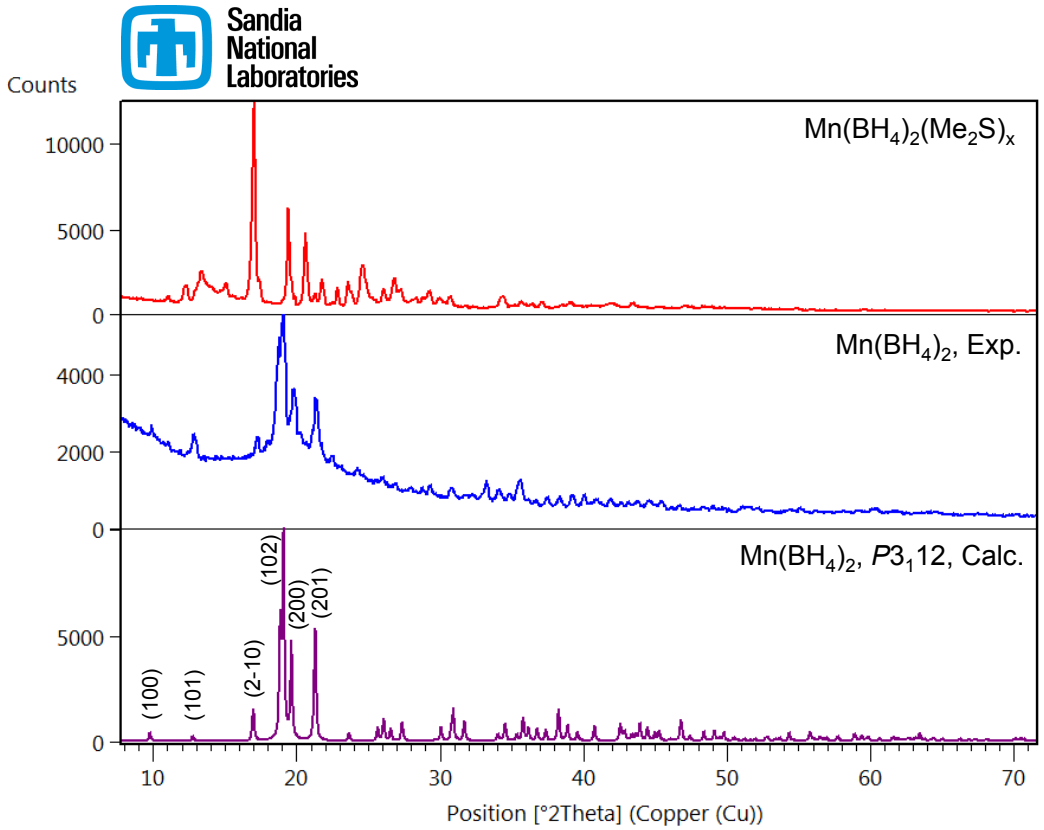

Figure 16. X-ray diffraction analysis of $Mn(BH_4)_2$ synthesis. Top (red) trace $Mn(BH_4)_2$-$(S(CH_3)_2)_x$ adduct; middle (blue) isolated $Mn(BH_4)_2$; bottom (purple) trace calculated pattern for $Mn(BH_4)_2$.

4.2 Synthesis of the mixed-metal borohydrides $Mg_{1-x}Mn_x(BH_4)_2$: The $MgMn(BH_4)_4$ material with a nominal Mg:Mg ratio of 1:1 was isolated in pure form. The synthesis was performed using a new procedure which involves the reaction of a mixture of equimolar amounts of Mg(*n*-Bu)$_2$ and Mn(*n*-Bu)$_2$ with borane-dimethylsulfide adduct in heptane. The as-synthesized powder is dried by removing excess solvent and Me_2S in vacuum upon mild heating. The solvent and dimethylsulfide removal procedure is critical in obtaining a pure material, as low temperature leads to a material which contains significant amounts of sulfur (according to elemental

analysis), while heating in vacuum over 100 °C leads to partial decomposition of the material. The as-synthesized mixed-metal Mg-Mn borohydride was characterized by means elemental analysis and Fourier transform infra-red (FTIR) spectroscopy. The elemental analysis shows a boron content of 29.8% and a hydrogen content of 10.93%, close to the calculated 31.19% and 11.63% for B and H in $MgMn(BH_4)_4$.

The FTIR spectra of $Mg(BH_4)_2$, $Mn(BH_4)_2$ and the newly-synthesized $MgMn(BH_4)_4$ are shown in Figure 17. The measurements were performed on an Agilent Cary-630 FTIR spectrometer in attenuated total reflectance (ATR) mode. The ATR method avoids possible contamination issues associated with the use of KBr in pellets; furthermore, it allows the sample measurements inside an argon glovebox. In the spectral region analyzed (500 – 4000 cm^{-1}), there are both BH_4^- bending (≈1000-1500 cm^{-1}) and B-H stretching modes (≈2000-2500 cm^{-1}). The position of the broad B-H stretching mode dependents on the metal ion, with the band observed at 2285 cm^{-1} for $Mg(BH_4)_2$, 2159 cm^{-1} for $Mn(BH_4)_2$ and 2207 cm^{-1} for $MgMn(BH_4)_4$. It is interesting to note that the FTIR spectra of $Mg(BH_4)_2$ and $Mn(BH_4)_2$ are quite similar, while the position of the stretching and bending bands in $MgMn(BH_4)_4$ is in-between those measured in parent borohydrides.

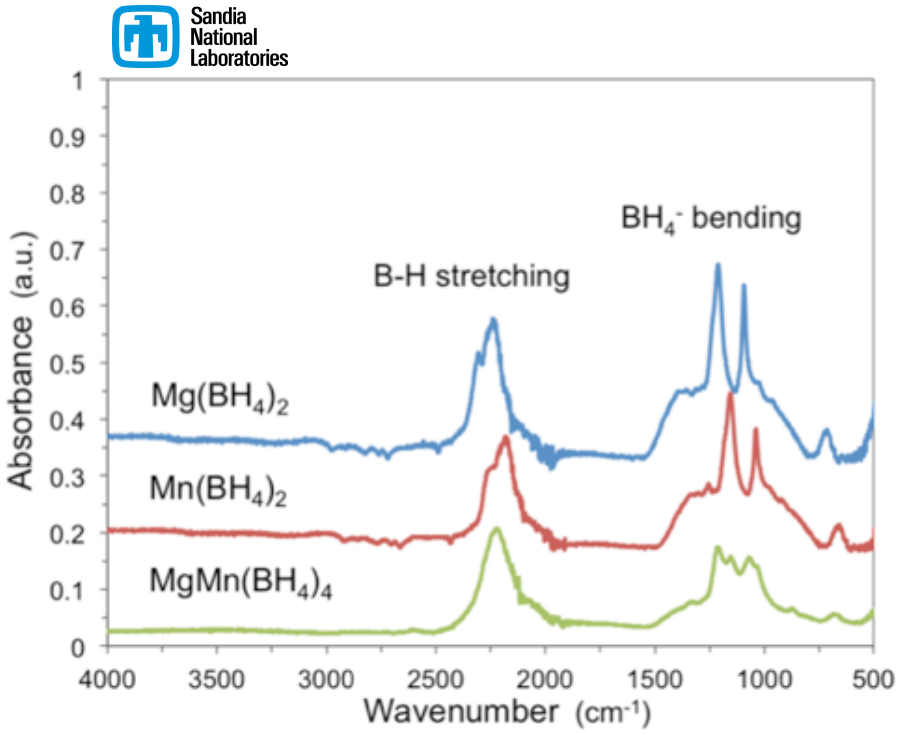

Figure 17. ATR FTIR spectra of $Mg(BH_4)_2$, $Mn(BH_4)_2$ and $MgMn(BH_4)$.

Material with a 1:1 metal ratio was further characterized by x-ray diffraction (XRD). The XRD pattern of the solvent-free $Mg_{0.5}Mn_{0.5}(BH_4)_2$ and the calculated patterns of various $Mg(BH_4)_2$ and $Mn(BH_4)_2$ phases are shown in Figure 18. The XRD data indicates a mixed-metal phase, and not a physical mixture of the two borohydride materials. The measurements were performed using a Empyrean X-ray diffractometer equipped with a PIXcel^{3D} detector and operated at 45 kV and 40 kA using Cu *Kα* radiation (λ= 1.5418 Å). A mixed-metal borohydride $Mg_{1-x}Mn_x(BH_4)_2$ material with x = 0.1 was also synthesized (data not shown). The synthesis was also scaled to a level of ~1 gram in order to enable characterization of the dehydrogenation behavior, as described below.

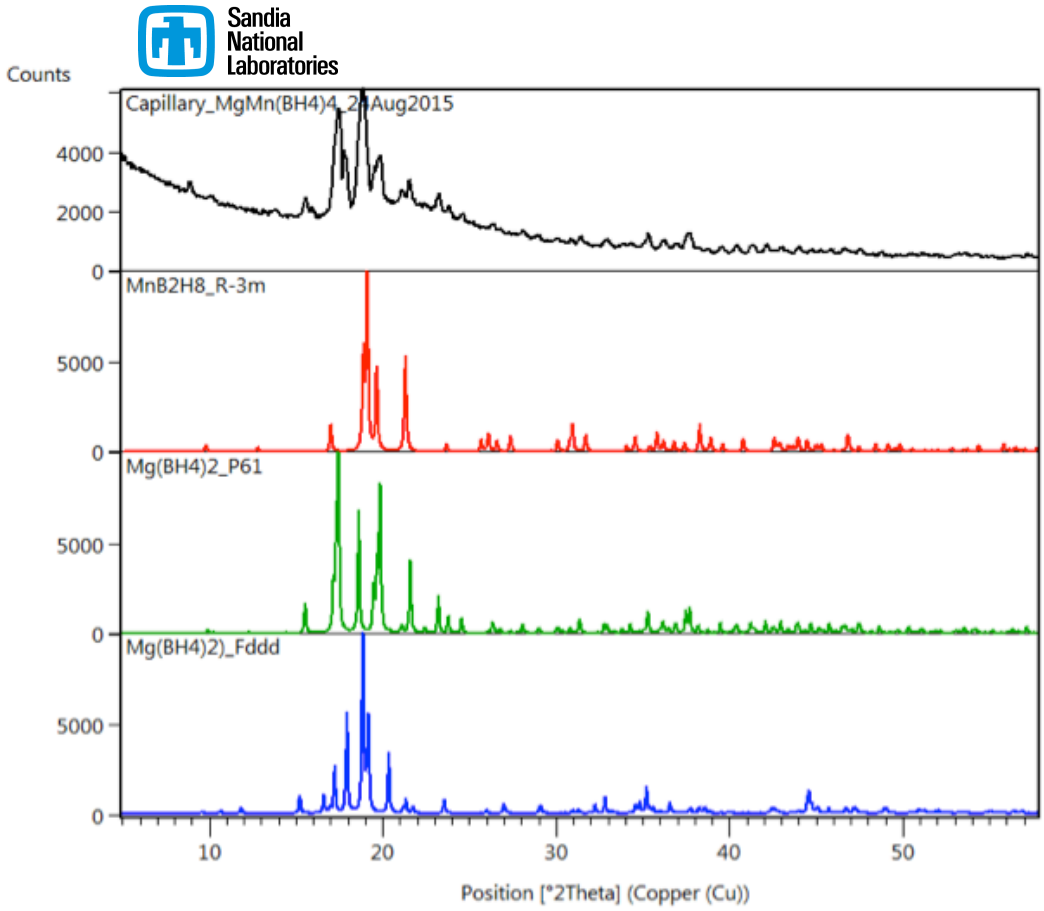

Figure 18. The measured XRD pattern of $Mg_{0.5}Mn_{0.5}(BH_4)_2$ and the calculated patterns of various $Mg(BH_4)_2$ and $Mn(BH_4)_2$ phases.

4.3 Hydrogen cycling of Mg/Mn mixed metal borohydride: The as-synthesized solvent-free $Mg_{0.5}Mn_{0.5}(BH_4)_2$ material was transferred into a stainless steel sample holder, which was subsequently attached to a Sieverts apparatus. A thermocouple was placed in the center of the sample holder for accurate temperature measurements during the experiments. Pressure changes during the dehydrogenation and rehydrogenation of the samples were quantified with calibrated pressure transducers and recorded using a Lab View-based software program. During the dehydrogenation step the temperature was ramped from ambient to ≈ 350 °C, then maintained at this temperature for up to 4 hours (Figure 19). Hydrogen capacity data are presented as weight % with respect to the $Mg_{0.5}Mn_{0.5}(BH_4)_2$ weight, assuming H_2 is the only gaseous product of the dehydrogenation reaction. In comparison to bulk $Mg(BH_4)_2$ (9) the kinetics of $Mg_{0.5}Mn_{0.5}(BH_4)_2$ decomposition are much faster. Preliminary residual gas analysis (RGA) measurements confirm H_2 is the major gaseous product (*m/z*=2), with small amounts of diborane (*m/z* = 24-27 and 12-15) being formed as well. Without accounting for RGA sensitivities, the amount of diborane was ~2.5 mol%.

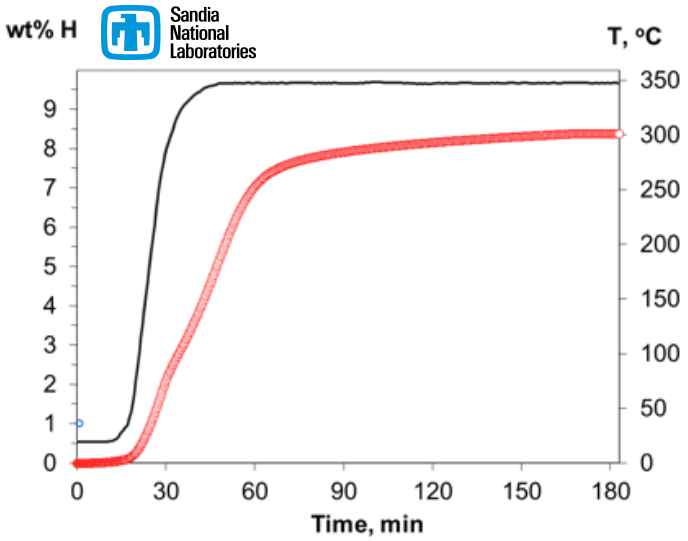

Figure 19. Sieverts hydrogen desorption data for $Mg_{0.5}Mn_{0.5}(BH_4)_2$. The temperature trace is shown in black, while the red trace indicates hydrogen content.

A small (~0.02 g) sample of the mixed metal borohydride $MgMn(BH_4)_4$ from an initial small scale synthesis at Sandia National Laboratories was delivered to HRL for hydrogen cycling. This sample is much smaller than those typically used (~0.4 to 2 g) in the HRL Sieverts apparatus. Therefore, a small sample vessel and the smallest desorption volume was used. In addition, prior to running the $MgMn(BH_4)_4$ sample, a ~0.02 g sample of AlH_3 was run to test the accuracy of the apparatus for samples with masses of 0.02 g and containing 5 wt% to 10 wt% hydrogen. The results (not shown) confirmed the capacity of the AlH_3 (7.8 wt%) measured previously on a much larger (~0.6 g) sample. The results for the $MgMn(BH_4)_4$ sample, a sample of pure gamma $Mg(BH_4)_2$ also synthesized at Sandia and a sample of $Mg(BH_4)_2$ milled with $0.03MnCl_2$ are shown in Figure 20.

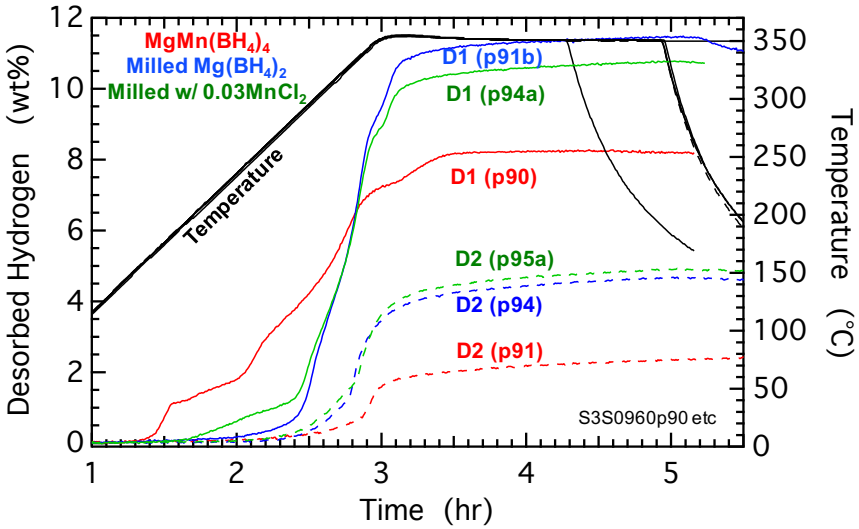

Figure 20. Dehydrogenation during hydrogen cycling of the mixed metal borohydride $MgMn(BH_4)_4$. Two dehydrogenation cycles are shown (D1-p90 and D2-p91). For comparison, two cycles are shown for milled $Mg(BH_4)_2$ (D1-p91b and D2-p94) and $Mg(BH_4)_2$ milled with 0.03 $MnCl_2$ (D1-p94a and D2-p95a). Hydrogenations were performed in ~100 bar H_2 at 300 °C for 10 hr.

Dehydrogenation of the mixed metal borohydride begins at ~150 °C (1.5 hr), although the sharp initial feature is likely residual solvent, not hydrogen. Several steps are seen with a final capacity of ~8 wt%. This capacity is ~70% of the theoretical capacity of 11.6 wt%. After hydrogenation under 100 bar H_2 at 300 °C for 10 hr, the capacity on the second cycle was only 2.2 wt%. While this capacity is much greater than the capacity possible from only the Mg component (1.4 wt%, theoretically for a 1:1 Mg:Mn ratio) it represents a significant reduction from the first cycle. In addition, the low temperature steps are absent with the onset of significant dehydrogenation beginning at ~ 300 °C. As expected, the pure $Mg(BH_4)_2$ sample has a much higher capacity (11.5 wt%, 78% of the theoretical 14.8 wt%). However, the kinetics are much slower with significant dehydrogenation only above ~250 °C. With addition of $0.03MnCl_2$, the kinetics improve slightly at low temperatures while, as expected because of the added weight, the capacity decreases. On the second cycles the capacities are ~4.5 wt%, which are ~2x the capacity for the $MgMn(BH_4)_4$ sample. Inclusion of the $MnCl_2$ actually improves the capacity slightly relative to the pure $Mg(BH_4)_2$ despite the added weight. For both pure $Mg(BH_4)_2$ and $Mg(BH_4)_2$ with added $MnCl_2$, the second cycle capacities are greater than the capacity possible from only the Mg component, 3.7 wt%.

To test whether a single or multiple phases are formed upon thermal decomposition of $Mg_{0.9}Mn_{0.1}(BH_4)_2$, we decomposed the material at 580 °C in an evacuated stainless steel vessel. We previously demonstrated that under these conditions $Mg(BH_4)_2$ yields pure and crystalline MgB_2. The XRD pattern of the as-decomposed $Mg_{0.9}Mn_{0.1}(BH_4)_2$ material, shown in Figure 21, confirms that the material displays *d*-spacing values characteristic to Mn-doped MgB_2 in P_6/mmm, with some peak broadening due to alloying. The SEM image (Figure 21, inset) of the product reveals large agglomerates of several microns in size.

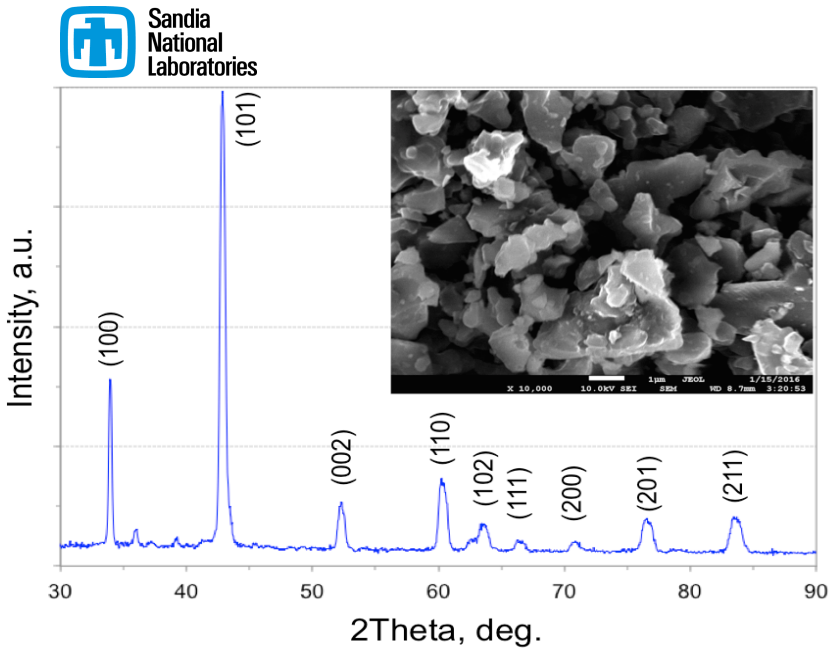

Figure 21. XRD pattern of the product of thermal decomposition of $Mg_{0.9}Mn_{0.1}(BH_4)_2$. The inset shows an SEM image of the product.

Energy-dispersive X-ray spectroscopy (EDX) measurements confirm that the as-decomposed $Mg_{0.9}Mn_{0.1}(BH_4)_2$ material is composed mainly of Mn, Mg and B, with only traces of oxygen, as shown in Figure 22. The EDS data, coupled with the XRD and SEM results indicate that the 9:1 Mg:Mn borohydride decomposes into a single ternary boride material.

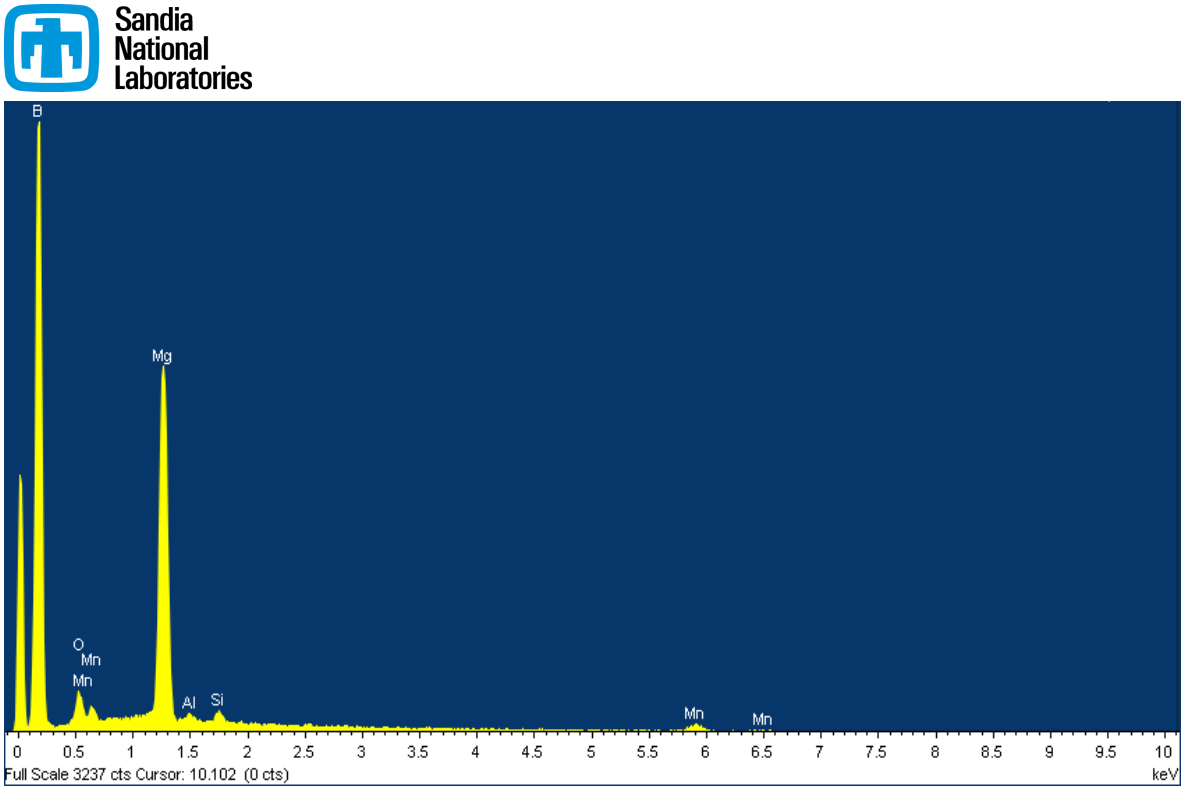

Figure 22. EDS spectrum of the as-decomposed $Mg_{0.9}Mn_{0.1}(BH_4)_2$ material.

5. Accomplishment — synthesis and lithiated borane hydrogen cycling reaction of an alloy substrate: One of the possible substrate classes for hydrogen storage via lithiation or boranes is extended alloys. As described above (Figure 7), Li_7B_6 contains linear chains of B atoms surrounded by Li that could hydrogenate to a BH_x + LiH mixture. The alloy Li_7B_6 thus constitutes the dehydrogenated phase of a lithiated borane L-H exchange reaction hydrogen storage material. Thus we synthesized Li_7B_6 and investigated it hydrogen cycling behavior.

5.1 Synthesis of Li_7B_6: The synthesis described in Ref. 5 was followed. Approximately 2 g of a mixture of 6B + 8Li, containing 1 mole excess Li, was mixed in a glove box by spreading portions of the boron powder on an area of metallic Li foil and repeatedly folding and compressing until the mixture was uniform. The mixture was loaded into ½ inch OD 316 stainless steel tubing that was sealed with Swagelok end caps. The tube was heated in a furnace at 450 °C for 48 hr. Approximately 0.8 g was recovered. An XRD pattern is shown in Figure 23. The dominant peaks index well to a database pattern for $LiB_{0.9}$. This is within the phase field for the B_6Li_7 phase (equivalent to $LiB_{0.86}$), which as shown in Figure 7, exists over the range $B_{0.8}$ to $B_{1.0}$. As expected, given the starting excess of Li, there is unreacted Li metal. There is also an impurity of Li_2O, which may have been present in the Li source.

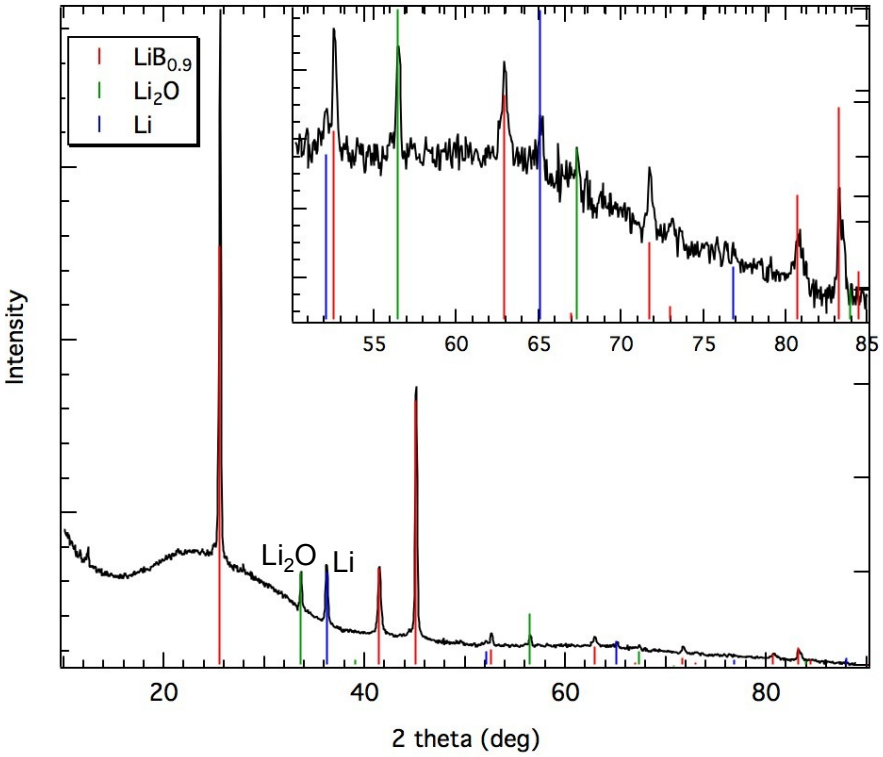

Figure 23. XRD pattern of synthesized B_6Li_7.

5.2 Hydrogenation/Dehydrogenation of alloy substrate Li_7B_6: A sample of the Li_7B_6 alloy was tested for hydrogen cycling. An example of the results is shown in Figure 24. The alloy sample was heated in ~100 bar of hydrogen up to 100 °C and ultimately up to 250 °C (Figure 24a). Significant hydrogen uptake of ~2.6 wt% was observed at 100 °C. Additional uptake, from 2.6 wt% to ~3.1 wt%, occurred as the sample was heated further to 250 °C. From a XRD analysis of the synthesized alloy, the sample was known to contain unreacted excess Li metal. Thus, the uptake at 100 °C could simply be hydrogenation of the unreacted Li. However, using phases sensitivities in the XRD database, the composition of the alloy sample was estimated to be $0.9Li_7B_6 + 0.08Li + 0.02Li_2O$. This composition would predict only ~0.08 wt% uptake from hydrogenation of the (0.08) unreacted Li. The much greater observed uptake suggests additional reaction(s), as discussed below. Upon dehydrogenation (Figure 24b), only a small amount of hydrogen desorbed, ~0.06 wt% during heating up to 250 °C.

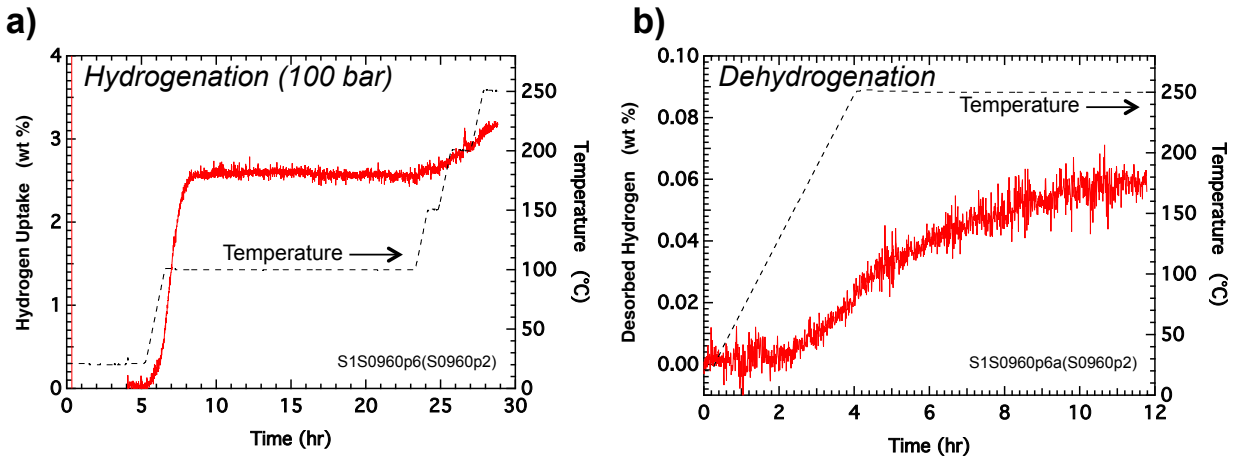

Figure 24. Hydrogenation a) and dehydrogenation b) of Li_7B_6 alloy.

The Li_7B_6 alloy sample was characterized after hydrogenation using FTIR and XRD; the results are shown in Figure 25. After hydrogenation, FTIR (Figure 25a) clearly indicates the formation of $[BH_4]^-$ from the three band fingerprint centered at ~2300 cm^{-1}. In addition, there is another clear B-H stretch not associated with $[BH_4]^-$. This additional B-H bonding may be associated with hydrogenation of, or hydrogen intercalation into, the Li_7B_6 alloy. The XRD pattern of the alloy after hydrogenation (Figure 25b) provides some support for a possible new intercalated phase. After hydrogenation, the diffraction peak for Li metal disappears and is replaced by two peaks from LiH. In addition, peaks for $LiBH_4$ appear confirming the FTIR data. As expected, the peak for Li_2O remains unchanged. The peaks for the Li_7B_6 alloy are particularly interesting. The as-synthesized alloy is characterized by three diffraction peaks at 25.6, 41.5, and 45.1 degrees 2-theta. Upon hydrogenation, the peaks at 25.6 and 45.1 degrees 2-theta are unchanged. However, the peak at 41.5 ° degrees 2-theta is missing. A peak at 38.7 degrees 2-theta appears suggesting that the 41.5 degrees 2-theta peak shifted down (green arrow, Figure 6b), as a result of lattice expansion. This shift could be caused by hydrogen intercalation into the Li_7B_6 alloy resulting in expansion in only one direction of the unit cell.

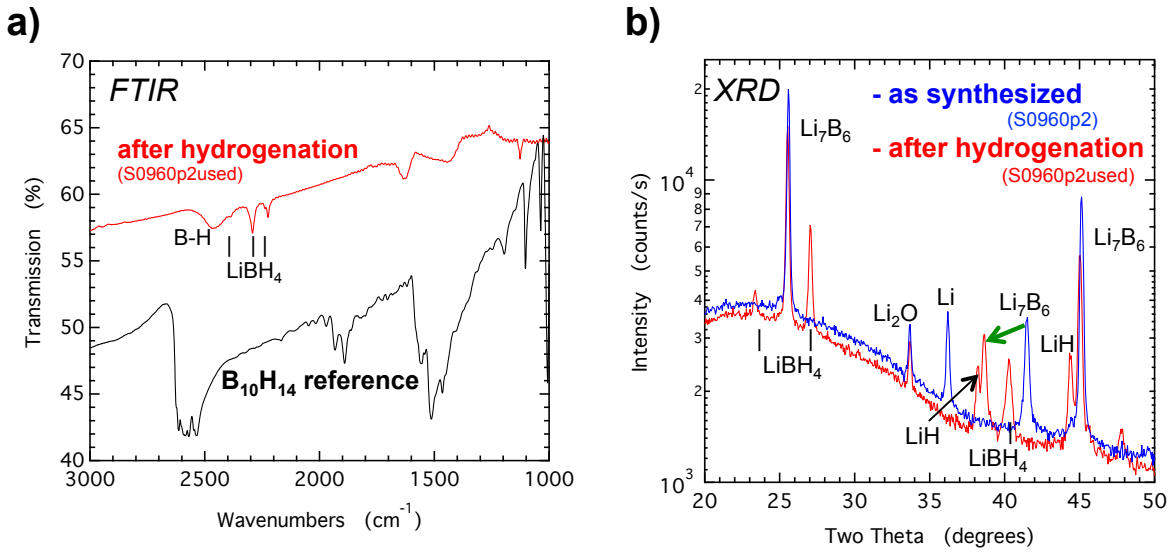

Figure 25. Characterization of hydrogenated Li_7B_6. a) FTIR. b) XRD

Hydrogen intercalated into Li boride alloys is not known. However, preliminary calculations performed at UMSL for alloys with the (very similar) composition of Li_8B_7 (in the P63/mmc structure) and Li_8B_7H with H on the B vacancy interstitial site that defines the structure, give diffraction patterns that agree well with the measured data. Specifically, the peaks at 25.6 and 45.1 degrees 2-theta were predicted and did not shift upon hydrogen intercalation while a peak at ~42 degrees 2-theta was predicted to shift to ~39.5 degrees 2-theta in good agreement with the data. However, the energetics of this structure are predicted to be very high and the structure is unstable to decomposition into $Li_8B_7 + 0.5H_2$. Two other interstitial sites for H with lower energies were found although these structures did not match the experimental diffraction pattern. If an intercalated composition of Li_7B_6H is assumed, the measured hydrogen uptake of ~3 wt% is approximately consistent with the following reaction:

$$0.9Li_7B_6 + 0.08Li + 1.6H_2\ (3.1\ wt\%) \rightarrow 0.8Li_7B_6H + 0.08LiH + 0.6LiBH_4.$$

It would be interesting to investigate this chemistry and the structure of the hydrogenated Li_7B_6 further. However, unfortunately, at least up to 250 °C, Li_7B_6H does not appear to be reversible.

6. Accomplishment — lithiated borane hydrogen cycling reactions of polymerized molecular borane substrates: The reaction of the molecular borane $B_{10}H_{14}$ with LiH has the potential to cycle >9 wt% hydrogen in a lithiated borane Li/H exchange reaction. Initial investigations were performed with $B_{10}H_{14}$ and LiH as well as Li metal (data not shown). However, sublimation of the $B_{10}H_{14}$ plagued the experiments and thus reactions with molecular $B_{10}H_{14}$ were abandoned. Similar issues were encountered with carboborane, *o*-$C_2B_{10}H_{12}$, despite its higher melting point (~260 °C compared to ~110 °C for $B_{10}H_{14}$). To overcome the issues associated with sublimation of molecular $B_{10}H_{14}$ while still trying to preserve the potentially high hydrogen capacity, a method to polymerize $B_{10}H_{14}$ was developed.

6.1 Polymerization of $B_{10}H_{14}$: Overall, the volatility of $B_{10}H_{14}$ and $C_2B_{10}H_{12}$ make them unsuitable for evaluation using standard Sieverts measurements. These molecular substrates could possibly be tested in a suitably high boiling point and reductively stable solvent under refluxing conditions. However, these measurements are currently beyond the scope of this effort. Rather, we decided, to try to polymerize the $B_{10}H_{14}$ to achieve a nonvolatile extended network borane substrate.

To polymerize the $B_{10}H_{14}$ substrate, ~1.5 g samples were heated in sealed stainless steel tubes (~8 cm^3) at 250 °C and 300 °C for 48 hr. Both samples changed from soft white molecular crystals to brittle yellow chunks. FTIR of the samples (Figure 26a) still show significant B-H bonding comparable to the $B_{10}H_{14}$ starting compound. Analysis of the retained hydrogen content perform at NIST is described below. An estimate was obtained from the mass of the 250 °C heat-treated tube before and after being cut open. From the mass loss, assumed to originate from loss of the evolved hydrogen, the final composition was $BH_{0.7}$. The FTIR also shows that most of the bands associated with vibrations of the B_{10} framework (~600 cm^{-1} to 1100 cm^{-1}) are gone, suggesting extensive crosslinking between molecules. The volatility of the 250 °C treated sample was also tested using TGA. As shown in Figure 26b, little mass loss was seen during 1 hour dwells at 250 °C and 300 °C.

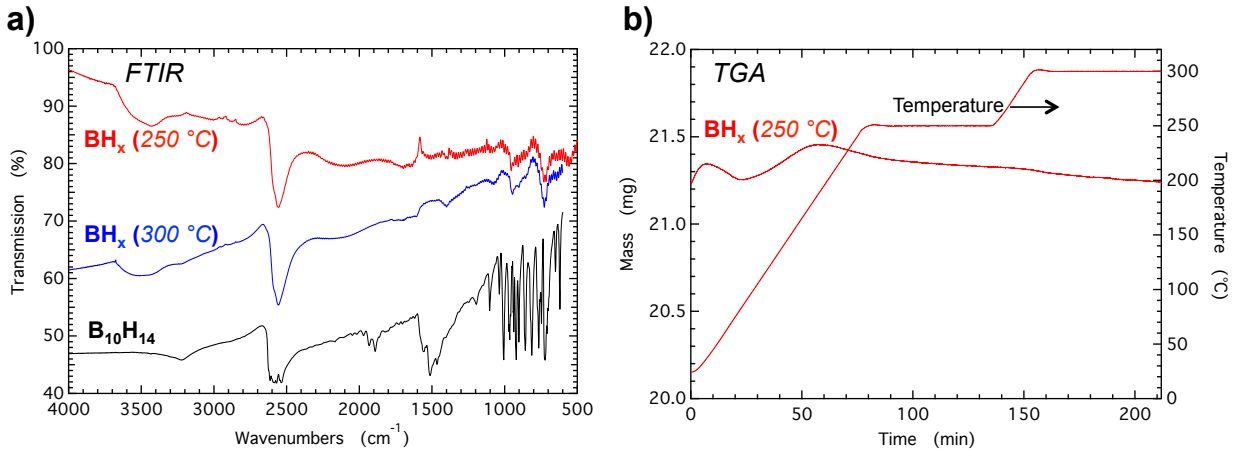

Figure 26. Characterization of polymerized $B_{10}H_{14}$. a) FTIR. b) TGA after treatment at 250 °C.

6.2 Hydrogen content of polymerized borane: Samples of polymerized $B_{10}H_{14}$ were prepared by thermal treatment in order to eliminate the volatile nature of molecular borane species. The hydrogen content of polymerized material was estimated by weight change to be $BH_{\sim 0.7}$. A more accurate analysis of the hydrogen content was determined by Terry Udovic at NIST using neutron prompt gamma-ray activation analysis. A sample treated at 300 °C for 48 hr was found to have a composition of $BH_{0.64 \pm 0.02}$. This composition agrees well with the rough estimate obtained by weighing. Two subsequent samples for which the weight was more carefully tracked gave compositions by weight change of $BH_{0.64}$ and $BH_{0.69}$.

6.3 Reaction of $B_{10}H_{14}$ polymerized at 300 °C with LiH: Polymerized $B_{10}H_{14}$ (300 °C, 48 hr) was mixed with LiH in the stoichiometry $BH_{0.64}$ + LiH and milled at 400 rpm for 20 hr. The 1st and 2nd hydrogen desorption cycles are shown in Figure 27. On the 1st cycle, ~0.35 wt% hydrogen desorbs. After hydrogenation in 100 bar H_2 at 250 °C for 1 hr, ~0.2 wt% was desorbed on the 2nd cycle. Although some hydrogen cycling is observed, the capacity is small and, more importantly, the dehydrogenation temperature is high with desorption beginning above ~300 °C.

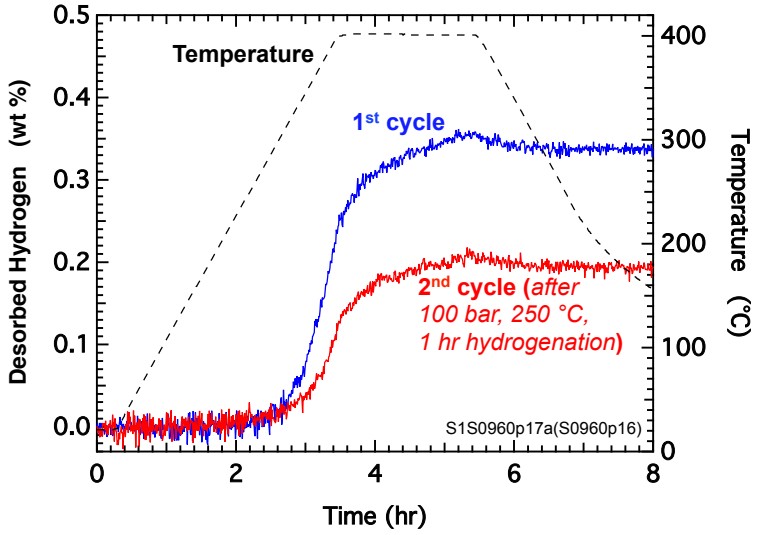

Figure 27. Dehydrogenation during hydrogen cycling in a 300 °C polymerized $B_{10}H_{14}$ milled with 10LiH.

To compared with the results in Figure 27, a sample of $B_{10}H_{14}$ polymerized at 300 °C for 48 hr and then milled at 200 rpm for 0.5 hr with and without 10LiH containing 3 at% Pd was studied. As described below the gentler milling conditions and lower temperature cycling were used to avoid formation of LiBH4. In addition, Pd was incorporated as a potential catalyst. The results are shown in Figure 28. The first and second cycle dehydrogenation behaviors are compared with and without LiH. The first cycle (D1) capacity for the sample milled with LiH is ~0.3 wt%. This is similar to the capacity shown for the sample in Figure 27, despite the lower temperature perhaps because of the Pd and because less $[BH_4]^-$ was formed during milling. On the second cycle (D2), 45% of the capacity was retained. The capacity on the third (D3) cycle is similar. Without added LiH, the first cycle capacity was <0.1 wt%. This result indicates that the desorbed hydrogen is resulting from a reaction between the polymerized borane and the LiH.

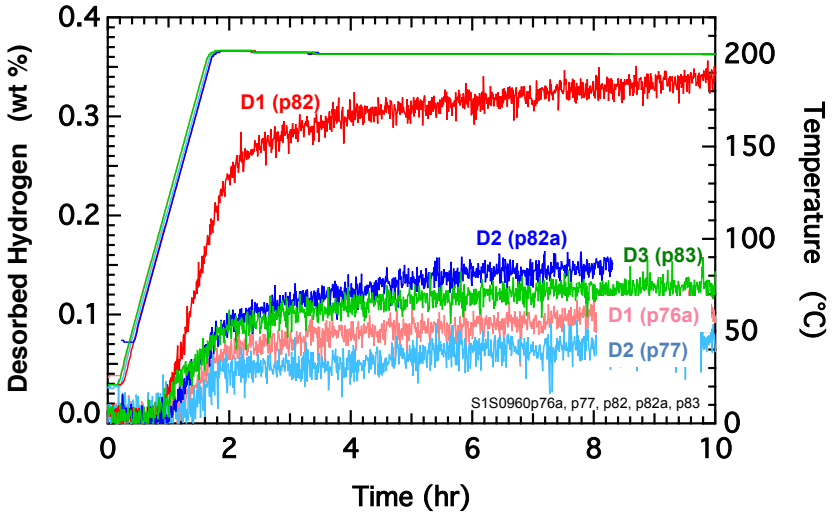

Figure 28. Dehydrogenation during hydrogen cycling of a polymerized mixture of $B_{10}H_{14}$ with and without 10LiH. Three dehydrogenation cycles are shown for a sample milled with LiH: D1 (p82), D2 (p82a), and D3 (p83). Two cycles are shown for a sample without LiH: D1 (p76a) and D2 (p77). Hydrogenations were performed in ~100 bar H_2 at 200 °C for 10 hr.

6.4 Reaction of $B_{10}H_{14}$ polymerized at 250 °C with LiH: To attempt to optimize the hydrogen cycling, a second polymerized sample was prepared by heating $B_{10}H_{14}$ at 250 °C for 48 hr. The hydrogen content, determined by weight loss, was $BH_{0.64}$. This sample was mixed in a 1:1 molar ratio with LiH and milled at 400 rpm for 1 hr. Four desorption cycles are shown in Figure 29. On the 1st cycle, significant dehydrogenation occurs at ~100 °C reaching 0.5 wt% at 250 °C. A separate run (data not shown) showed that 0.35 wt% could be desorbed at 150 °C. However, after hydrogenation in ~80 bar at 250 °C for 2 hr, no further dehydrogenation occurred on the 2nd desorption cycle until above 300 °C. At temperatures up to 400 °C, ~1 wt% H_2 was reversible over 4 cycles.

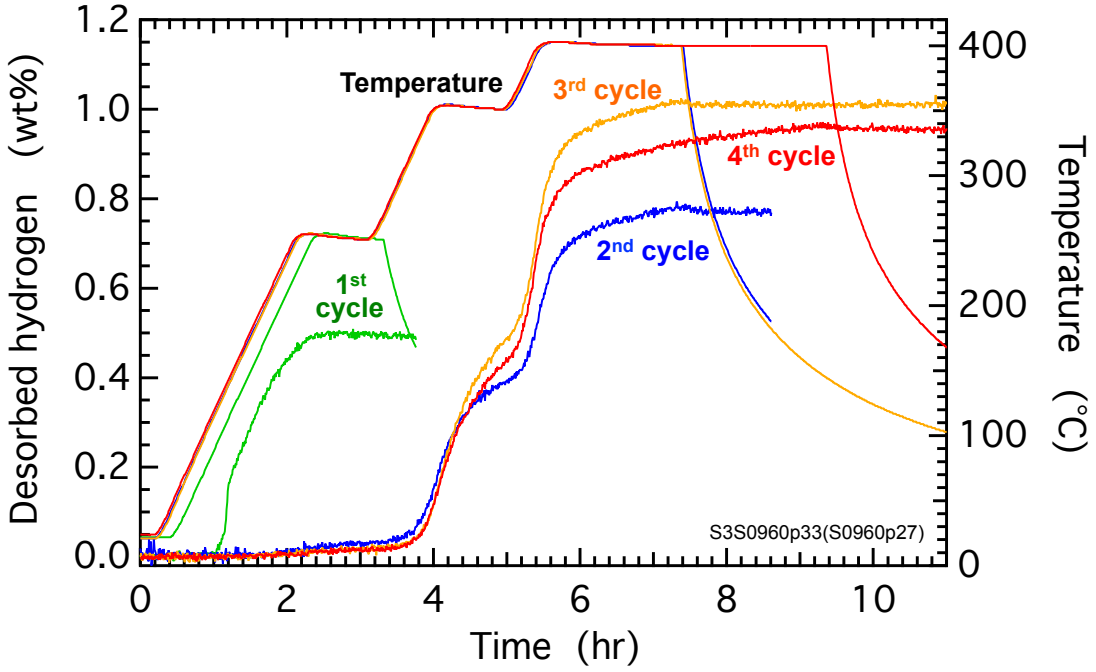

Figure 29. Dehydrogenation during hydrogen cycling in a 250 °C polymerized borane $B_{10}H_{14}$ milled with 10LiH.

As a control experiment for the polymerized $B_{10}H_{14}$ + 10LiH sample shown in Figure 29, a sample of $B_{10}H_{14}$ that was polymerized at 250 °C was cycled without added LiH; the results are shown in Figure 30. At temperatures < 250 °C little dehydrogenation occurs, ~0.1 wt% H_2. This result indicates further that the low temperature desorption for the $B_{10}H_{14}$ + 10LiH mixture likely originates from a reaction between LiH and the polymerized borane. In contrast, the similarity of the dehydrogenations at higher temperatures when accounting for the 60% mass fraction of BH_x in the $B_{10}H_{14}$ + 10LiH mixture, suggests that this hydrogen may originate from further decomposition of the polymerized borane and not reaction with the LiH.

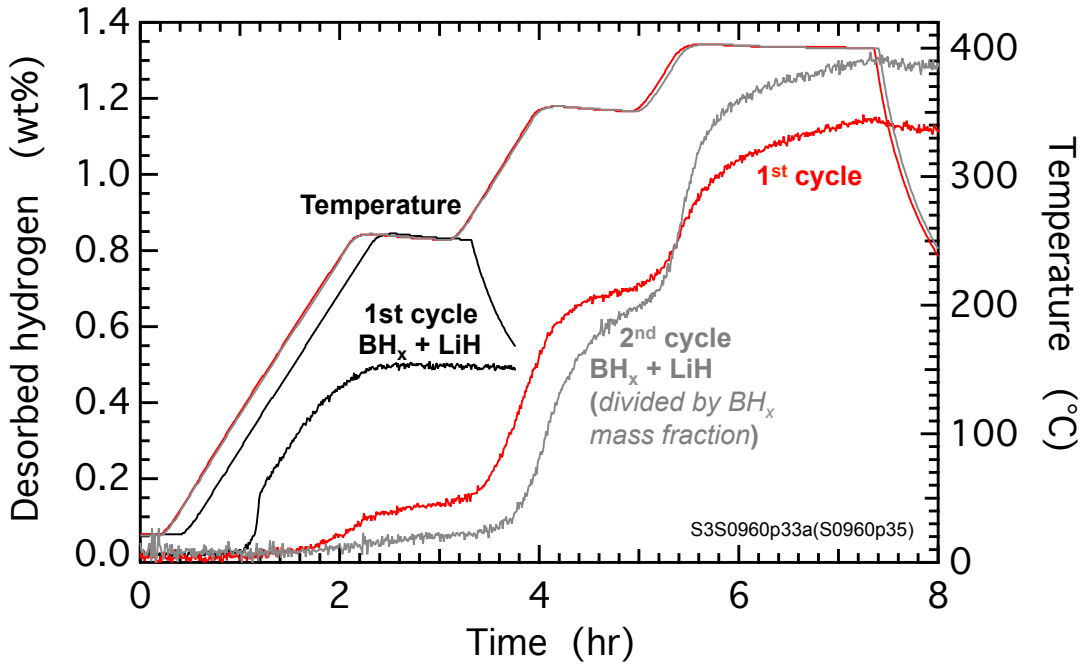

Figure 30. First dehydrogenation of a 250 °C polymerized $B_{10}H_{14}$ compared with a 250 °C polymerized borane BH_x + LiH mixture scaled to account for the 60% mass fraction of BH_x.

6.5 FTIR analysis of polymerized $B_{10}H_{14}$ + Li reactions: As described above, the low temperature dehydrogenation feature seen in several polymerized borane/LiH reactions was not reversible. However, in several of the hydrogenation experiments (data not shown) there appeared to be uptake of hydrogen. To understand the fate of this hydrogen, FTIR spectra were obtained. These spectra were obtained from a sample polymerized with $AlCl_3$ in order to include Cl as a dopant. The hydrogen cycling behavior of doped samples is described further below. As shown in Figure 31, it appears that formation of $[BH_4]^-$ was occurring. After polymerization, a single broad B-H stretch is seen at ~2520 cm-1, as expected for a disordered borane framework. However, already upon milling with LiH (400 rpm, 1 hr) a clear signature of $[BH_4]^-$ anions can be seen. The broad B-H stretch also shifts slightly to 2495 cm-1. The origin of this shift is not clear but could be associated with the formation of $[B_{12}H_{12}]^{2-}$ anions. After cycling at 200 °C consisting of a 1st cycle desorption, a 1st cycle hydrogenation (~80 bar), and a 2nd cycle desorption (4 hr), the intensity of the $[BH_4]^-$ stretches grows considerably. It appears that $LiBH_4$ is being formed at 200 °C and is not decomposing during the 2nd 200 °C desorption cycle (as is known for $LiBH_4$). Note: we do not think this behavior results from the $AlCl_3$ addition. Although the low temperature formation of $LiBH_4$ in these materials is interesting, the intent of this approach is to avoid $[BH_4]^-$ formation because it entails breaking of B-B bonds together with B atom diffusion.

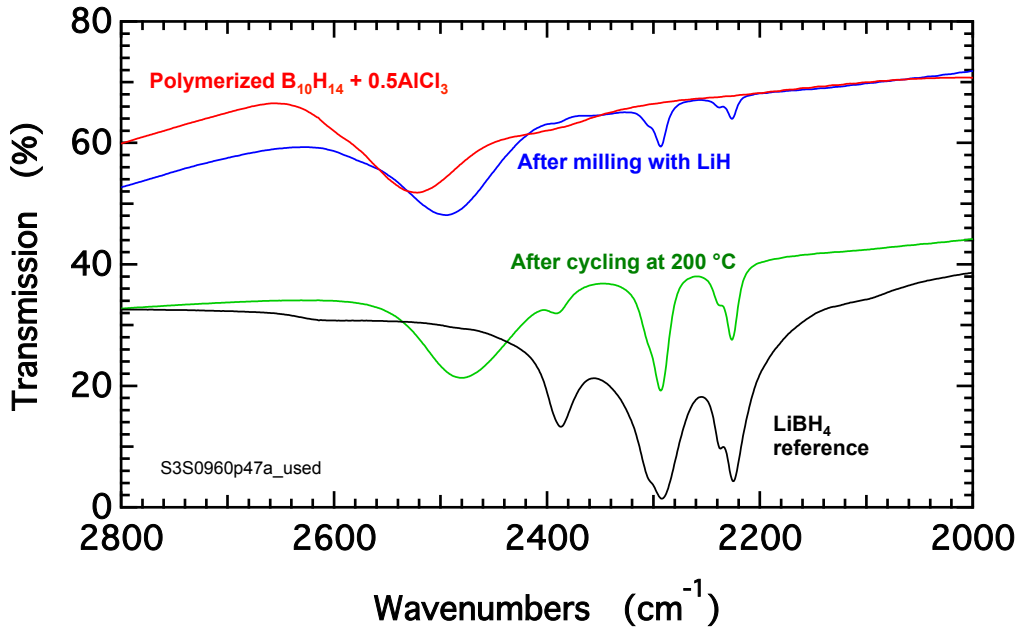

Figure 31. FTIR spectra in the B-H stretching region. Spectra for 250 °C polymerized $B_{10}H_{14}$ + 0.5 $AlCl_3$, after milling with 10LiH, after dehydrogenation, hydrogenation, and dehydrogenation at 200 °C, and LiBH4 reference.

As shown in Figure 31 for $BH_x/AlCl_3$ + LiH, some $[BH_4]^-$ forms during milling with LiH. This high-energy milling is used to intimately mix the polymerized borane and LiH phases in order to provide good interfacial contact between the phases where subsequent Li/H exchange reaction might occur. However, it appears that the mixing may be too energetic, leading to break down of the borane framework. To check how easily $[BH_4]^-$ forms, a BH_x + LiH mixture was milled under longer and increasingly energetic conditions. Analysis of the milled mixtures and comparison to 400 rpm, 1 hr milled $BH_x/B_2(OH)_4$ + LiH is shown in Figure 32. Like the $BH_x/AlCl_3$ mixture mentioned above, $BH_x/B_2(OH)_4$ was studied to look for effects of oxygen doping. After hand mixing, milling at 100 rpm for 15 min, and milling at 200 rpm for 15 min, there is no indication of the most intense fingerprint band for $[BH_4]^-$. After milling at 200 rpm for a total of 1 hr a small absorption at 2295 cm^{-1} can just barely been seen. Milling at 400 rpm for 15 min yields small but clear $[BH_4]^-$ fingerprint bands at 2295 cm^{-1} and 2225 cm^{-1}. In addition, milling the $BH_x/B_2(OH)_4$ + LiH mixture at 400 rpm for 1 hr produces significant $[BH_4]^-$ very similar to that seen for $BH_x/AlCl_3$ + LiH in Figure 31. Mechanical mixing may not be appropriate for this reaction. A solution-based process where LiH is solubilized and precipitated is described below.

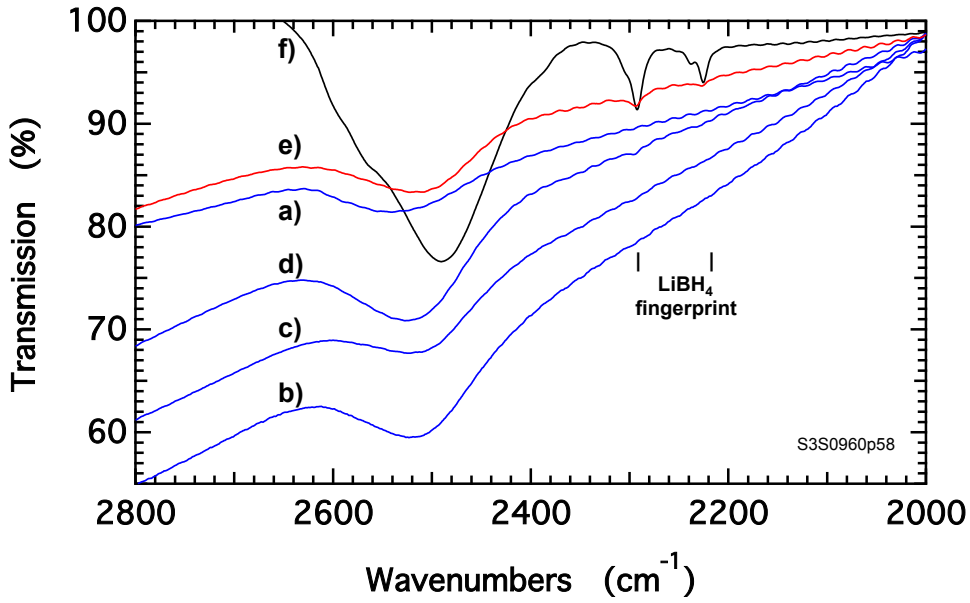

Figure 32. FTIR spectra in the B-H stretching region. Spectra for a) 250 °C polymerized $B_{10}H_{14}$ after a) hand mixing with 10 LiH; and then b) milling at 100 rpm for 15 min; c) milling at 200 rpm for 15 min; d) milling at 200 rpm for a total of 1 hr; e) milling at 400 rpm for 15 min; and f) 250 °C polymerized $B_{10}H_{14}$ + 0.5 $B_2(OH)_4$ after milling with 11LiH at 400 rpm for 1 hr.

6.6 Differential scanning calorimetry of the H/Li exchange reaction: Polymerized borane samples prepared at HRL were sent to University of Missouri for differential scanning calorimetry (DSC) measurements to determine the thermal properties at elevated temperatures. The samples were prepared as follows:

- p13: $B_{10}H_{14}$, polymerized at 300 C
- p13 + 10LiH, hand mixed under argon
- p71: $B_{10}H_{14}$, polymerized at 300 C for 48 hrs and mechanically milled in a planetary mill at 200 rpm for 30 min
- p80: sample p71 + 10 mole equivalents of (LiH + 0.03 Pd), milled at 200 rpm for 30 min.
- p81: $B_{10}H_{14}$ + $LiNH_2BH_3$ + 0.03Pd polymerized at 300 C for 48 hrs and milled at 200 rpm for 30 min
- p87: sample p81 + 10 mole equivalents of (LiH + 0.03Pd), milled at 200 rpm for 30 min.

Reference spectra for polymerized $B_{10}H_{14}$ with no additives is shown in Figure 33 (sample p13, red trace). The data is featureless on heating, with a slight endothermic bend in the baseline. The same sample with 10 mol% LiH shows a sharp endothermic transition between 300 °C and 350 °C. The process resulting in this transition has not been determined. Features on cooling are artifacts attributed to the sample pan in the DSC.

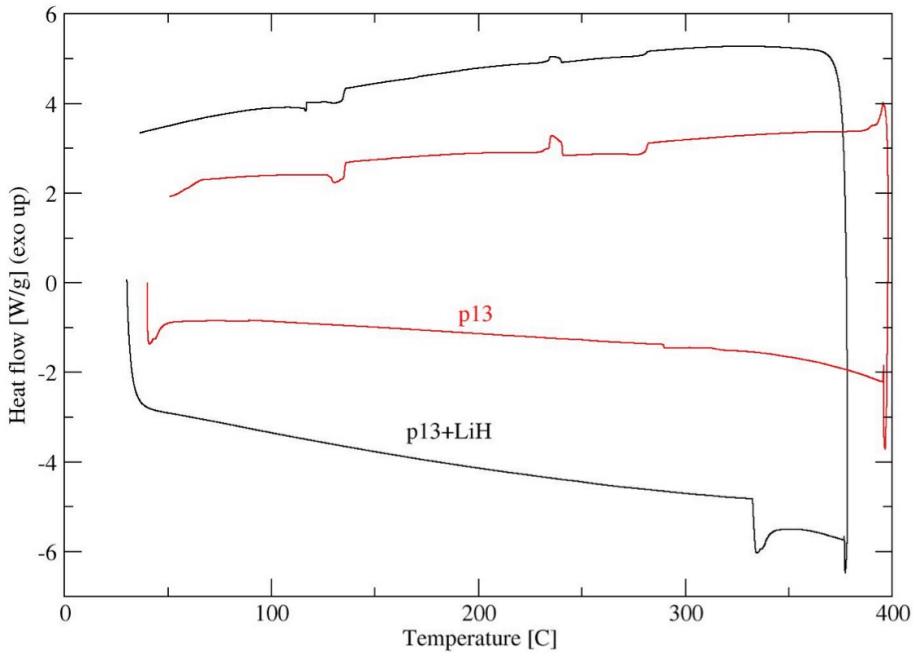

Figure 33. DSC of polymerized $B_{10}H_{14}$ (p13, red trace), and $B_{10}H_{14}$+10LiH. The heating cycle is the lower portion of each trace. Data was collected using a TA Instruments calorimeter at a scan rate of 10 °C/min.

Sample p71 is similar to sample p13 except that it was mechanically milled. Sample p80 was milled under more mild milling conditions than previous samples to suppress formation of $LiBH_4$. Samples p81 and p87 were prepared to investigate any changes in the thermal properties of nitrogen addition to polymerized decaborane. DSC data shown in Figure 34 was taken using a Perkin-Elmer DSC7 using hermetically sealed aluminum pans and a scan rate of 10 °C/min. Sample p71 is similar to p13 in Figure 33. The DSC trace for p71 is generally featureless with a slight change in the baseline over the temperature range from 0 to 250 °C. The addition of LiH and 0.03Pd results in exothermic behavior between 100 °C and 200 °C, followed by a sharp endothermic transition just above 200 °C. This is similar to the behavior of sample p13+LiH, but with a significantly lower temperature for the endothermic transition, which has not been identified. Samples p81 and p87 are prepared with polymerized $B_{10}H_{14}$ + $LiNH_2BH_3$ to incorporate nitrogen. The pure polymerized material (p81) has no distinct features and is similar to pure polymerized $B_{10}H_{14}$. The spikes in the data around 225 °C are likely gas escaping from the pan or pan thermal contact changes as the hermetically sealed pan expands with temperature. Most notable is the DSC trace for sample p87, composed of sample p81+10LiH and 0.03 Pd. This sample shows a significant endothermic transition at 150 °C, a lower onset transition than shown in sample p80. This is consistent with calculated trends, although the endothermic reactions remain unidentified in these materials. Overall, the DSC data support an exothermic evolution of hydrogen from the BH_x + LiH reaction.

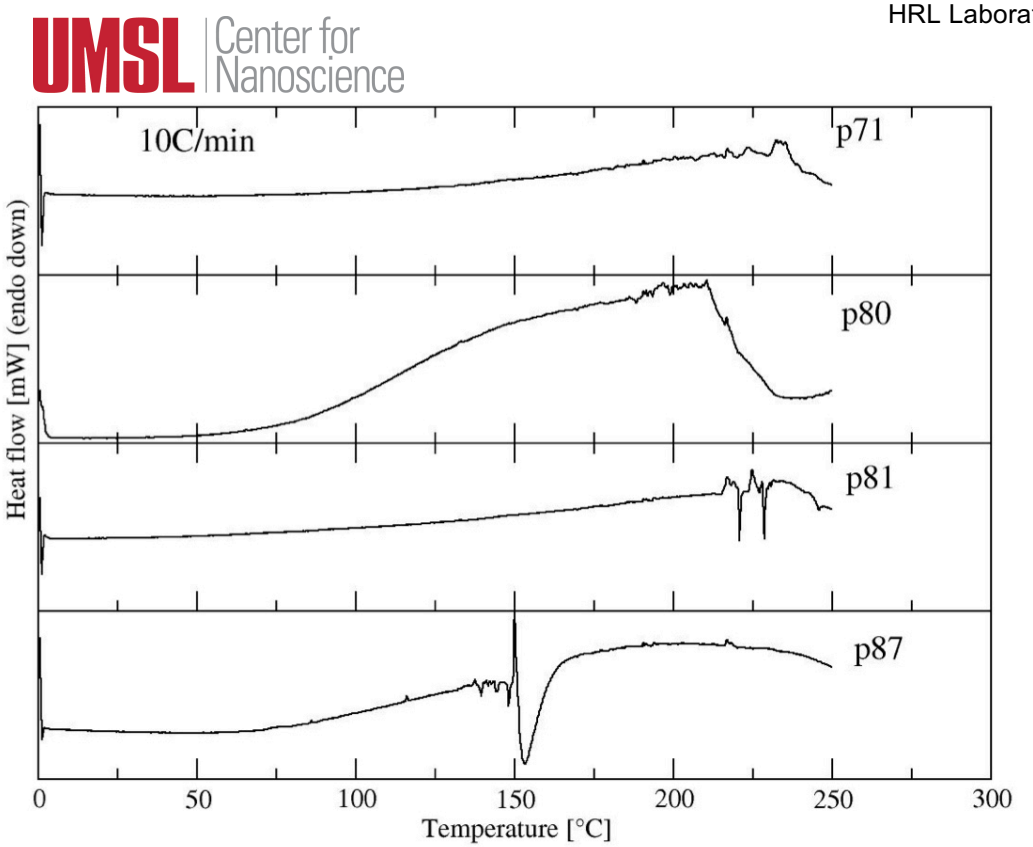

Figure 34. DSC traces of polymerized $B_{10}H_{14}$ with LiH, with and without nitrogen-containing additives.

6.7 H/Li exchange reaction in $B_{10}H_{14}$ polymerized at 300 °C mixed with LiH in solution: As described previously, milling LiH with polymerized borane led to the formation of $[BH_4]^-$ anions. This necessitated reducing the milling speed and time. An alternative to milling was investigated. A sample of polymerized borane was hand mixed with LiH. Then a 2 molar solution of triethylborane (BEt_3) in diethyl ether was added to dissolve the LiH by formation of $LiBEt_3H$. A 2x mole ratio BEt_3 to LiH was used to ensure full reaction of the LiH. The ether and excess BEt_3 were allowed to evaporate at room temperature and then the mixture was heated to 100 °C to decompose the $LiBEt_3H$ with evaporation of the BEt_3. Reforming the LiH from a homogeneous solution presumably led to a well dispersed mixture of polymerized borane and LiH with good interfacial contact. Hydrogen cycling of this mixture is shown in Figure 35, compared to a mixture prepared by milling. The sample prepared by solution mixing shows a sharp desorption at ~100 °C. However, this is likely residual ether, not hydrogen. At higher temperatures the kinetics and capacity are similar to the mechanically milled sample. On the second cycle, the capacity is poor, much lower than for the milled sample.

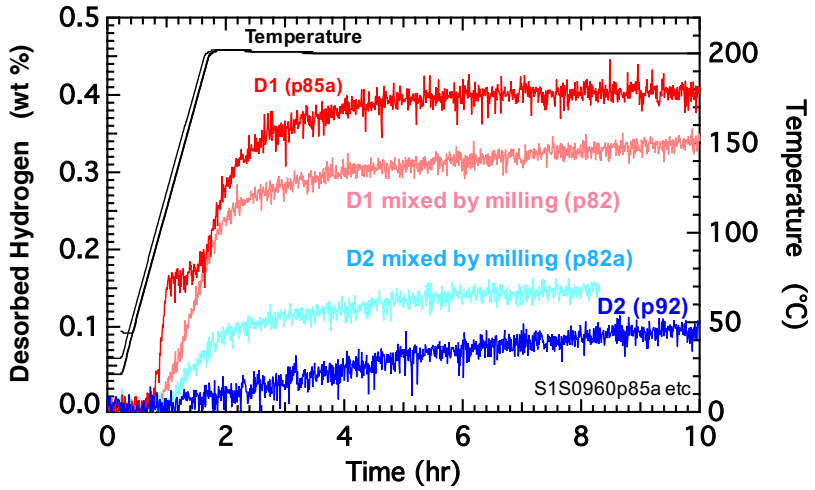

Figure 35. Dehydrogenation during hydrogen cycling of a mixture of polymerized $B_{10}H_{14}$ mixed with 10LiH by a solution process. Two dehydrogenation cycles are shown (D1-p85a and D2-p92). For comparison two cycles for pure polymerized $B_{10}H_{14}$ prepared by milling are shown (D1-p82 and D2-p82a). Hydrogenations were performed in ~100 bar H_2 at 200 °C for 10 hr.

6.8 H/Li exchange reaction in $BH_{0.36}$ nanoparticles mixed with LiH in solution: To compared with the polymerized borane, hydrogenated nanoparticles of boron with a composition of $BH_{0.36}$ were obtained from Professor Scott Anderson at the University of Utah. Rather than milling these particles with LiH, which could destroy them, LiH was mixed with the particles using the solution process described above. To account for the lower hydrogen content of the nanoparticles compared with the polymerized borane ($BH_{0.36}$ versus $BH_{\sim 0.7}$), a $BH_{0.36}$ + 0.5LiH mixture was prepared, again with a 2x excess of BEt_3. Hydrogen cycling of the final mixture is shown in Figure 36. The kinetics of the dehydrogenation are similar to those for the polymerized borane. However, the capacities are lower reflecting the lower hydrogen content of the nanoparticles. The capacity was stable from the second to the third although very low, only <0.1 wt%.

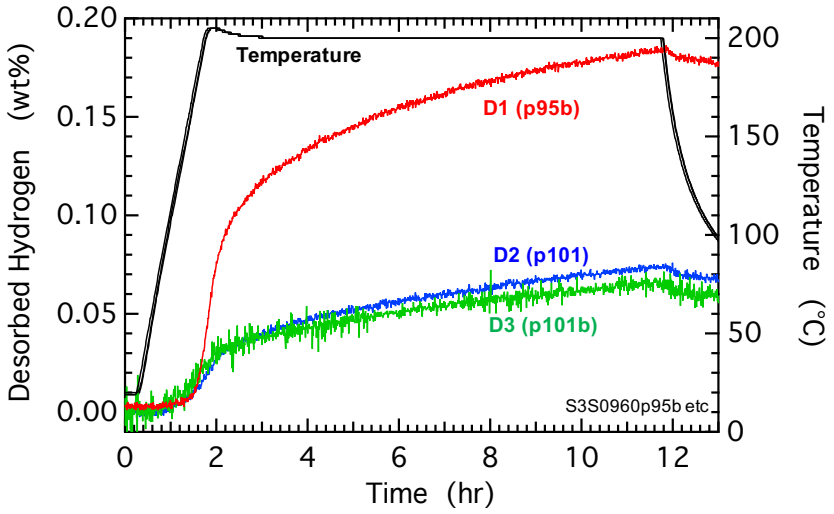

Figure 36. Dehydrogenation during hydrogen cycling of a hydrogenated boron nanoparticles $BH_{0.36}$ mixed with 0.5LiH by a solution process. Three dehydrogenation cycles are shown (D1-p95b, D2-p101. and D3-p101b). Hydrogenations were performed in ~100 bar H_2 at 200 °C for 10 hr.

6.9 H/Li exchange reaction in $B_{10}H_{14}$ polymerized with heteroatoms dopants: The results shown above indicate only small capacities with likely exothermic reaction. In order to possibly improve the capacities, especially on second and subsequent cycles, borane polymerized with heteroatom dopants was surveyed. The dopants tried include Al, O, N, Cl, and C.

Although computational results indicated that electropositive heteroatoms would lower the H/Li exchange energy and both DSC and computational results suggest that the exchange energy is already likely too low, ie possibly exothermic, incorporation of Al as a heteroatom into polymerized $B_{10}H_{14}$ was studied. This study was undertaken, despite the trend described above, in part because the aluminum source was aluminum hydride (AlH_3) which is a very direct and chemically straightforward source for incorporation of aluminum. AlH_3 was obtained from Savanna River National Laboratory. It was measured to have a hydrogen content of ~8 wt% hydrogen. A sample was prepared by polymerizing at 300 °C a milled mixture of $B_{10}H_{14}$ + AlH_3. After polymerization, LiH was mixed in by mechanical milling at 200 rpm for 0.5 hr. Note that the reduced milling speed and time (lowered from 400 rpm for 1 hr) were used to avoid the milling induced formation of $[BH_4]^-$ anions. The hydrogen cycling behavior is shown in Figure 37. On the first dehydrogenation cycle the capacity is lower than for pure polymerized $B_{10}H_{14}$ without any additional heteroatoms. Furthermore, the dehydrogenation temperature appears unchanged. On the second cycle the capacity is similar to the pure polymerized $B_{10}H_{14}$ indicating a slightly higher second cycle capacity retention, 50% vs. 45%, however, the absolute capacity is small, only ~0.12 wt%.

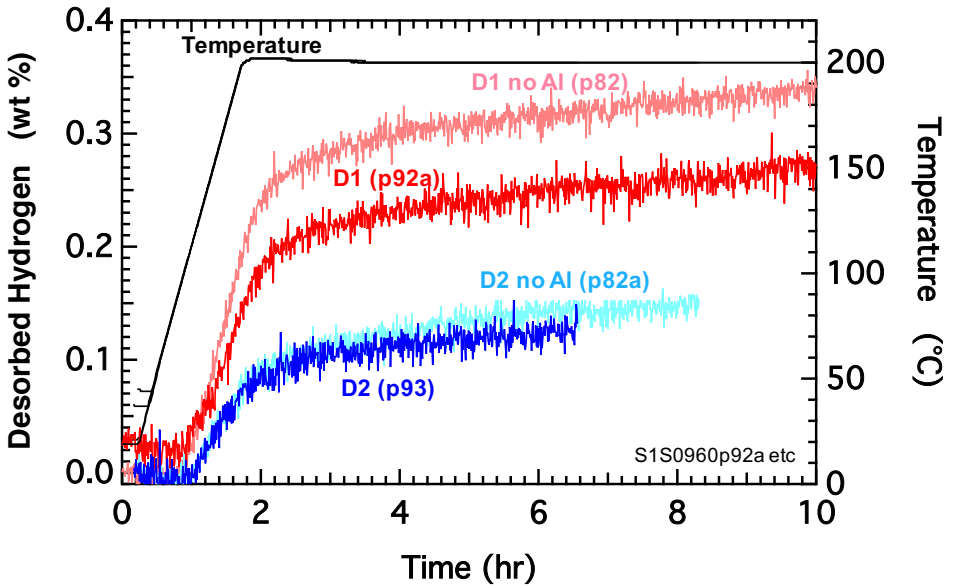

Figure 37. Dehydrogenation during hydrogen cycling of a polymerized mixture of $B_{10}H_{14}$ + AlH_3 milled with 10(LiH + 0.03Pd). Two dehydrogenation cycles are shown (D1-p92a and D2-p93). For comparison two cycles for pure polymerized $B_{10}H_{14}$ without added aluminum are shown (D1-p82 and D2-p82a). Hydrogenations were performed in ~100 bar H_2 at 200 °C for 10 hr.

Although still containing destabilizing O heteroatoms, the hydrogen cycling behavior of a mixture of $B_{10}H_{14}$ + $0.5B_2(OH)_4$ + 0.3Pd polymerized at 300 °C for 48 hr and then mechanically

milled with 11LiH at 200 rpm for 0.5 hr is shown in Figure 38. The ~3 at% Pd with respect to boron was added as a potential catalyst. The milling speed and time were reduced from 400 rpm and 1 hr, which prevented the formation of $[BH_4]^-$ anions (FTIR data not shown). In addition, the hydrogen cycling temperature was limited to 200 °C. The amount of hydrogen desorbed on the first cycle (D1) was much less than that for polymerization at 250 °C, ~0.2 wt% vs. ~0.4 wt% However, there was ~50% capacity retention (~0.1 wt%) on the second (D2) and third (D3) cycles. Thus, although the absolute capacity was lower, the reversible retained capacity was significantly higher (~50% vs. <10%). We note that after the third dehydrogenation cycle (D3), characterization by FTIR still showed a clear signature from $[BH_4]^-$ anions, despite no initial $[BH_4]^-$.

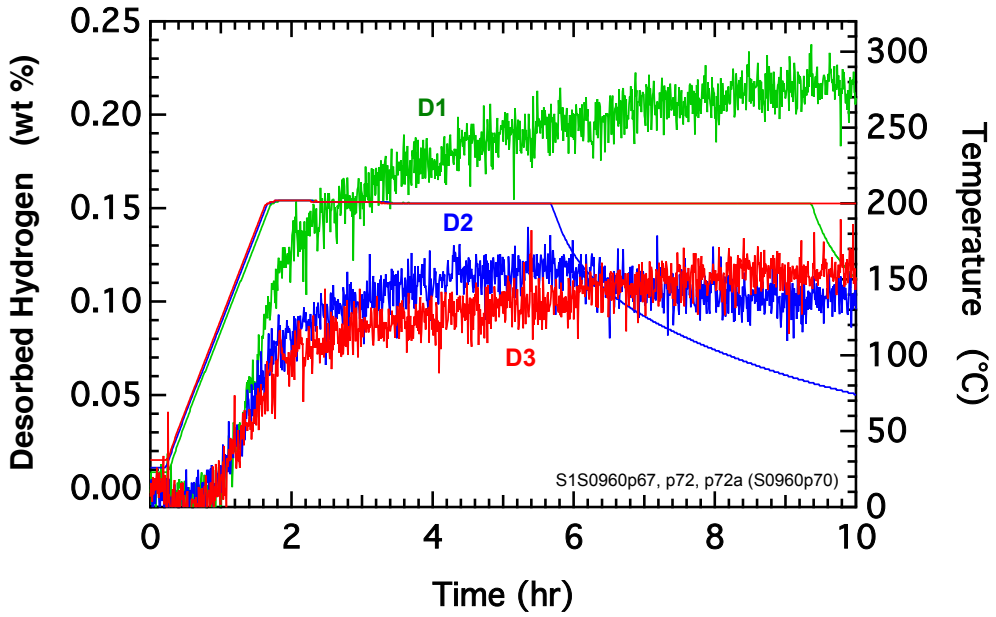

Figure 38. Dehydrogenation during hydrogen cycling of a polymerized mixture of $B_{10}H_{14}$ + 0.5$B_2(OH)_4$ + 0.3Pd milled with 10LiH. Three dehydrogenation cycles are shown (D1, D2, and D3). Hydrogenations were performed in ~100 bar H_2 at 200 °C for 10 hr.

To check whether the cycled hydrogen shown in Figure 38 might originate from the polymerized borane alone, a sample was prepared without LiH. The results are shown in Figure 39. As also shown, a repeat run with LiH gave very reproducible results. Without LiH, the capacity at 200 °C was <0.05 wt%. These results indicate that the hydrogen is resulting from reaction between the LiH and the polymerized borane.

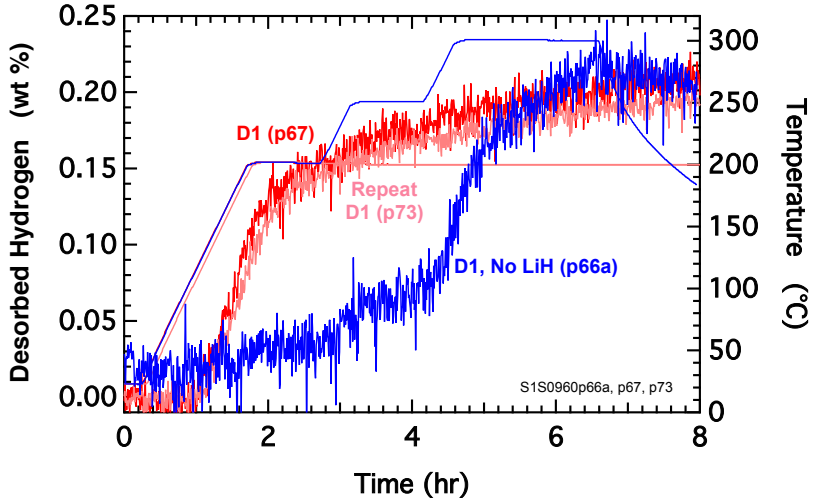

Figure 39. Dehydrogenation during hydrogen cycling of a polymerized mixture of $B_{10}H_{14}$ + 0.5$B_2(OH)_4$ + 0.3Pd with and without 10LiH. To illustrate reproducibility, dehydrogenation of two samples milled with 10LiH are shown: D1 (p67) and Repeat D1 (p73).

Earlier calculations predicted that the addition of nitrogen into the boron atom framework would stabilize the B-H bonds and increase the H/Li exchange enthalpy. Given that the enthalpies appear low, incorporation of nitrogen was studied. A sample was prepared by polymerizing at 300 °C a milled mixture of $B_{10}H_{14}$ + $LiNH_2BH_3$ + 0.3Pd. After polymerization, $[BH_4]^-$ was already detected by FTIR. This was no longer surprising knowing the propensity of $[BH_4]^-$ to form in milled samples containing Li. Hydrogen cycling was studied in samples subsequently milled (200 rpm, 0.5 hr) with and without LiH. The results are shown in Figure 40. The capacity is clearly higher with the added LiH. However, with the added nitrogen the capacity retention on the second cycle is lower, only ~33%.

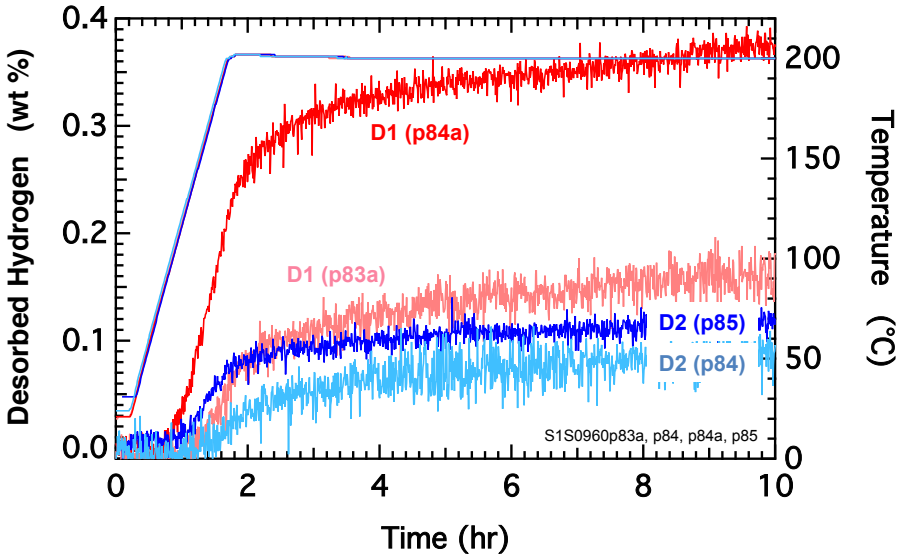

Figure 40. Dehydrogenation during hydrogen cycling of a polymerized mixture of $B_{10}H_{14}$ + $LiNH_2BH_3$ + 0.3Pd with and without 10LiH. Two dehydrogenation cycles are shown for a sample milled with LiH: D1 (p84a) and D2 (p85). Two cycles are shown for a sample without LiH: D1 (p83a) and D2 (p84). Hydrogenations were performed in ~100 bar H_2 at 200 °C for 10 hr.

Overall, for polymerized borane materials with added heteroatoms of Al, O, Cl (data not shown), or N at levels of ~0.1 heteroatom/B atom, no significant differences in the hydrogen cycling behavior was observed. In addition, attempts to incorporate carbon into the polymerized borane were unsuccessful. Additives expected to incorporate carbon, such as low molecular weight polyethylene appeared to form methane without carbon incorporation.

7. Accomplishment — computational assessment of ternary boride/mixed-metal borohydride compositions suitable for single phase hydrogen cycling: Density functional theory (DFT) methods were used to determine favorable ternary boride compositions. The prototype electrostatic ground state (PEGS) method was used to identify candidate mixed-metal borohydride phases. Together these calculations were used to determine possible pairs of ternary borides and mixed-metal borohydrides that could cycle hydrogen while maintaining single hydrogenated and dehydrogenated phases.

7.1 Assessment of Mg-transition metal ternary borides: Initial studies of ternary borides examined the energetics of alloying MgB_2 and transition metal borides to form ternary boride phases. Results for 1:1 and Mg rich 2:1 Mg:TM ratio reactions given by

$MgB_2 + (TM)B_2 \rightarrow Mg(TM)B_4$ (*Pbam*)

and

$2MgB_2 + (TM)B_2 \rightarrow Mg_2(TM)B_6$ (*Pbam*)

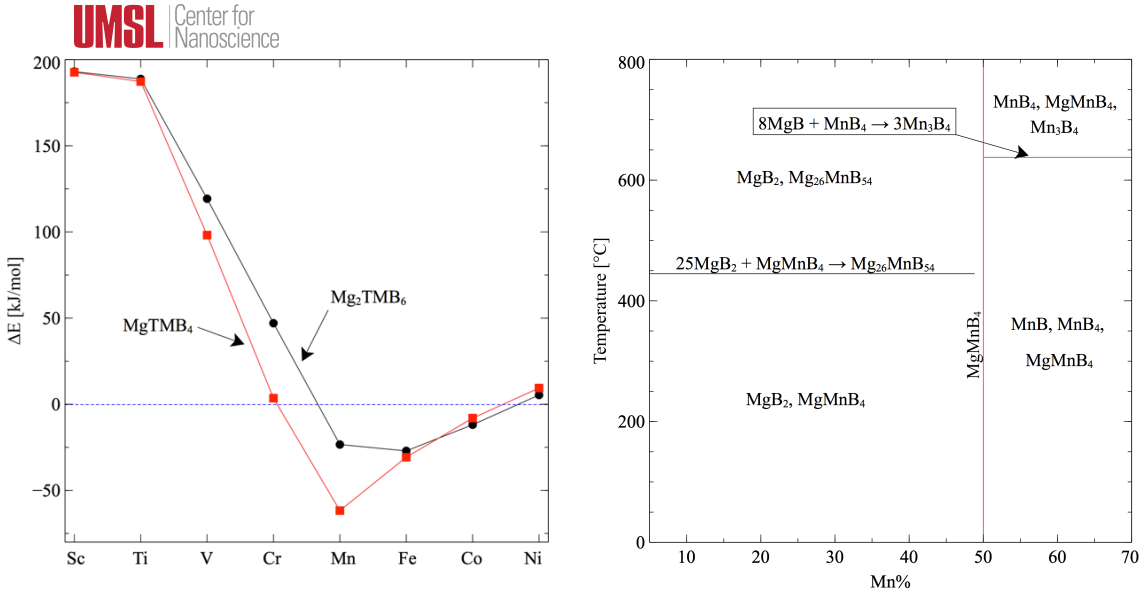

Figure 41. Predicted DFT energies of formation for ternary diborides (left panel). Calculated phase diagram for $Mn_{(1-x)}Mg_xB_2$ system (right panel).

are shown in Figure 41. The calculations were performed for T = 0 K including zero point energies (ZPE) with dE < 0 indicating a favorable reaction forming a stable ternary boride. For TM = Fe, Co, and Ni the diborides do not exist. For these reactions, elemental boron and the monoboride, ie, B + (TM)B, were substituted for $(TM)B_2$. The calculations indicate that TM = Mn, Fe, and Co have stable ternary borides with Mg. These results give support for the $Mg_{0.5}Mn_{0.5}B_2$ phase identified by milling (Figure 9).

Overall, these calculations suggest that stable Mg/TM ternary borides are likely for Mn, Fe, and Co and thus, if formed by dehydrogenation of a mixed metal borohydride they would not further disproportionate into multiple boride phases.

Above, stable ternary borides of Mg with the first row transition metals (TM) were considered for simple stoichiometric ratios of TM:Mg such as 1:1, 1:2, and 1:3, corresponding to 50 mol%, 33 mol%, and 25 mol% TM. Here, lower TM concentrations were investigated in the range of 5:27 (18.5 mol%) down to 1:27 (3.7 mol%). These compositions are considered to be solid solutions. Calculations were performed for a 3x3x3 supercell with the P6/mmm symmetry of MgB_2. The detailed stoichiometries were $Mg_{27-n}TM_nB_{54}$ for n = 1, 2, 3, 4, and 5. A schematic of the unit cell is shown in Figure 42.

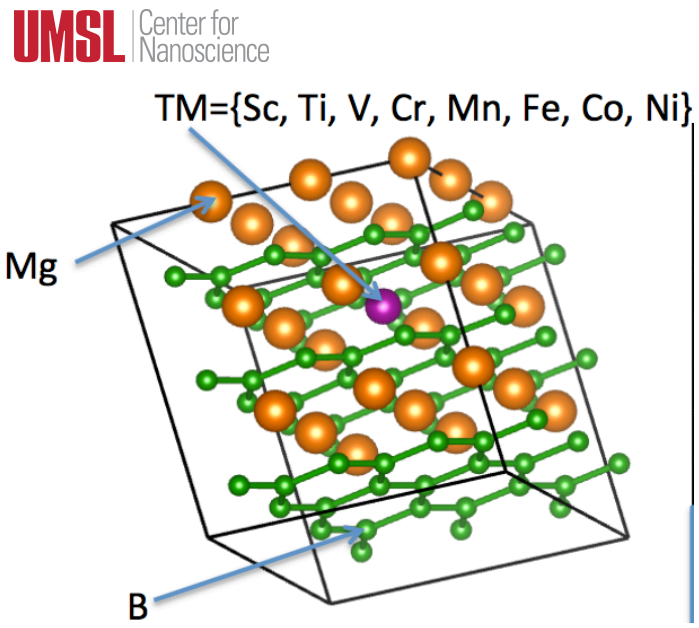

Figure 42. Model of $Mg_{26}TMB_{54}$ unit cell.

To assess the stability of the different compositions, a grand canonical linear programming (GCLP) minimization using all know phases including previously calculated phases was performed. A list of the phases used for TM = Sc is shown in Table 2.

UMSL Center for Nanoscience

Material	Symmetry	f.u.	*k*-points	E [eV/f.u.]	ZPE [eV/f.u.]
MgB_2	*P6/mmm*	1	16x16x16	-15.38	0.18
B	*R-3m*	36	4x4x2	-6.69	0.13
Mg	*P-3m1*	2	16x16x16	-1.52	0.02
Sc	$P6_3/mmc$	2	16x16x16	-6.18	0.02
ScB_{12}	*Fm-3m*	4	8x8x8	-89.25	1.50
ScB_6	*P1*	1	14x14x16	-48.06	0.74
ScB_2	*P6/mmm*	1	10x10x10	-22.13	0.21
$Mg_{26}ScB_{54}$	*P1*	1	2x2x2	-422.11	7.28
$Mg_{25}Sc_2B_{54}$	*P1*	1	2x2x2	-428.81	7.26
$Mg_{24}Sc_3B_{54}$	*P1*	1	2x2x2	-435.45	7.20
$Mg_{23}Sc_4B_{54}$	*P1*	1	2x2x2	-442.29	7.21
$Mg_{22}Sc_5B_{54}$	*P1*	1	2x2x2	-449.18	7.23
$MScB_4$	*Pbam*	4	6x2x10	-35.62	0.48
Mg_2ScB_6	*P1*	4	4x2x10	-51.08	0.74

Table 2. Phases used for GCLP minimization of the Mg-Sc-B system.

The GCLP minimization was used to generate a "phase profile" of the Mg-Sc-B system. This phase profile is shown in Figure 43. For this system, MgB_2 and ScB_2 are the only stable phases below 263 °C. As shown previously, the 1:1 phase is not stable for TM = Sc. Above 263 °C, the $Mg_{22}Sc_5B_{54}$ composition is predicted to be stable. Finally, above 350 °C, the $Mg_{26}ScB_{54}$ phase is predicted to be stable.

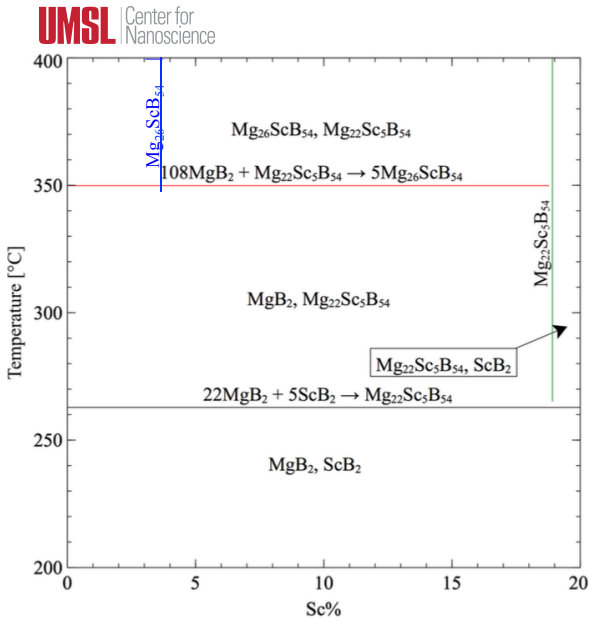

Figure 43. Phase profile for the Mg-Sc-B system.

7.2 Assessment of Mg-based mixed-metal borohydrides: Using PEGS structures, DFT calculations were performed to predict the energetics for dehydrogenation of mixed metal borohydrides. The calculations examined two borohydride compositions, $Mg(TM)(BH_4)_4$ and $Mg_2(TM)(BH_4)_6$ that dehydrogenate to ternary diborides according to the reactions

$Mg(TM)(BH_4)_4 \rightarrow Mg(TM)B_4$ (*Pbam*) + $8H_2$

and

$Mg_2(TM)(BH_4)_6 \rightarrow Mg_2(TM)B_6$ (*Pbam*) + $12H_2$

The transition metals used were Mn, Fe, and Co. Unit cell structures from PEGS calculations for the various borohydride compositions are shown in Figure 44.

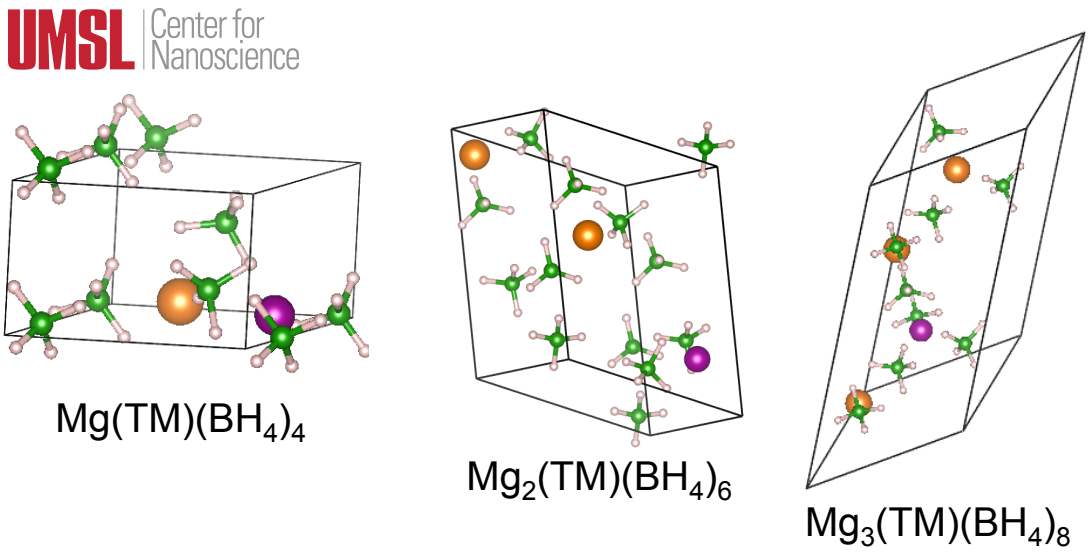

Figure 44. Unit cell structures from PEGS calculations for mixed metal borohydrides. Atom colors: boron (green); hydrogen (white), magnesium (yellow), and transition metal (purple).

The results of the calculations are shown in Tables 3 and 4. All of the borohydrides are unstable. For the $Mg(TM)(BH_4)_4$ composition, the dehydrogenation is predicted to be exothermic in all cases. Thus, these dehydrogenation reactions would not be reversible For the $Mg_2(TM)(BH_4)_6$ composition, the dehydrogenation is more positive but still slightly exothermic or approximately thermo-neutral for Mn. Including the entropy contribution from the evolved hydrogen gas, these reactions would also likely not be reversible.

UMSL Center for Nanoscience

TM	$MgTM(BH_4)_4$ [eV]	$MgTMB_4$ [eV]	H_2 [eV]	dE [eV/f.u.]	dE [kJ/mol H_2]
Mn	-88.51	-38.36	-6.53	-2.09	-25.14
Fe	-88.45	-37.45	-6.53	-1.23	-14.79
Co	-86.92	-36.19	-6.53	-1.50	-18.06

Table 3. Calculations for the dehydrogenation of $Mg(TM)(BH_4)_4$. Reaction energies (dE) are given in eV per formula unit (f.u.) and kJ/mol-H_2.

UMSL Center for Nanoscience

TM	$Mg_2TMB_6H_{24}$ [eV]	Mg_2TMB_6[eV]	H_2 [eV]	dE [eV/f.u.]	dE [kJ/mol H_2]
Mn	-131.55	-53.18	-6.53	0.03	+0.21
Fe	-130.97	-52.63	-6.53	-0.01	-0.05
Co	-129.46	-51.44	-6.53	-0.33	-2.66

Table 4. Calculations for the dehydrogenation of $Mg_2(TM)(BH_4)_6$. Reaction energies (dE) are given in eV per formula unit (f.u.) and kJ/mol-H_2.

Although the energetics of these reactions appear unfavorable for hydrogenation, the positive increase in energies between the $Mg(TM)(BH_4)_4$ and $Mg_2(TM)(BH_4)_6$ compositions suggest that higher Mg:TM ratios may be endothermic. To test this idea, the $Mg_3(TM)(BH_4)_8$ composition (see Figure 15) was studied for TM = Mn. Single phase dehydrogenation of $Mg_3Mn(BH_4)_8$ would yield Mg_3TMB_8. However, Mg_3MnB_8 was found to be unstable with respect to decomposition into $Mg_2MnB_6 + MgB_2$. The predicted decomposition energy is -0.53 eV/f.u. This suggests that $Mg_3(TM)(BH_4)_8$ would not dehydrogenate into a single phase boride. Although not single phase, the energetics for the dehydrogenation reaction

$$Mg_3Mn(BH_4)_8 \rightarrow Mg_2MnB_6 + MgB_2 + 16H_2$$

was calculated. The results, shown in Table 5, predict a favorable endothermic energy. Between the compositions studied or perhaps at even higher Mg:Mn ratios may be a composition that has both an endothermic dehydrogenation and a stable ternary boride.

UMSL Center for Nanoscience

$Mg_3Mn(BH_4)_8$	Mg_2MnB_6 [eV]	MgB_2 [eV]	H_2 [eV]	dE [eV/f.u.]	dE [kJ/mol H_2]
-174.14	-53.18	-15.21	-6.53	1.28	+7.73

Table 5. Calculations for the dehydrogenation of $Mg_3(TM)(BH_4)_8$ into Mg_2MnB_6 + MgB_2. Reaction energies (dE) are given in eV per formula unit (f.u.) and kJ/mol-H_2.

Experimental reports indicate that there is Mg/Mn mixing at a 1:1 ratio in the structure for $Mg_{0.5}Mn_{0.5}(BH_4)_2$,(10) and that the resulting crystal structure is related to the experimentally observed $Mn(BH_4)_2$ in spacegroup $P3_1$.(11) Powder XRD of our synthesized sample does not match the experimental diffraction pattern for $Mn(BH_4)_4$ in space group $P3_1$, or the PEGS-predicted structures in space group I-4m2 (see Figure 45).

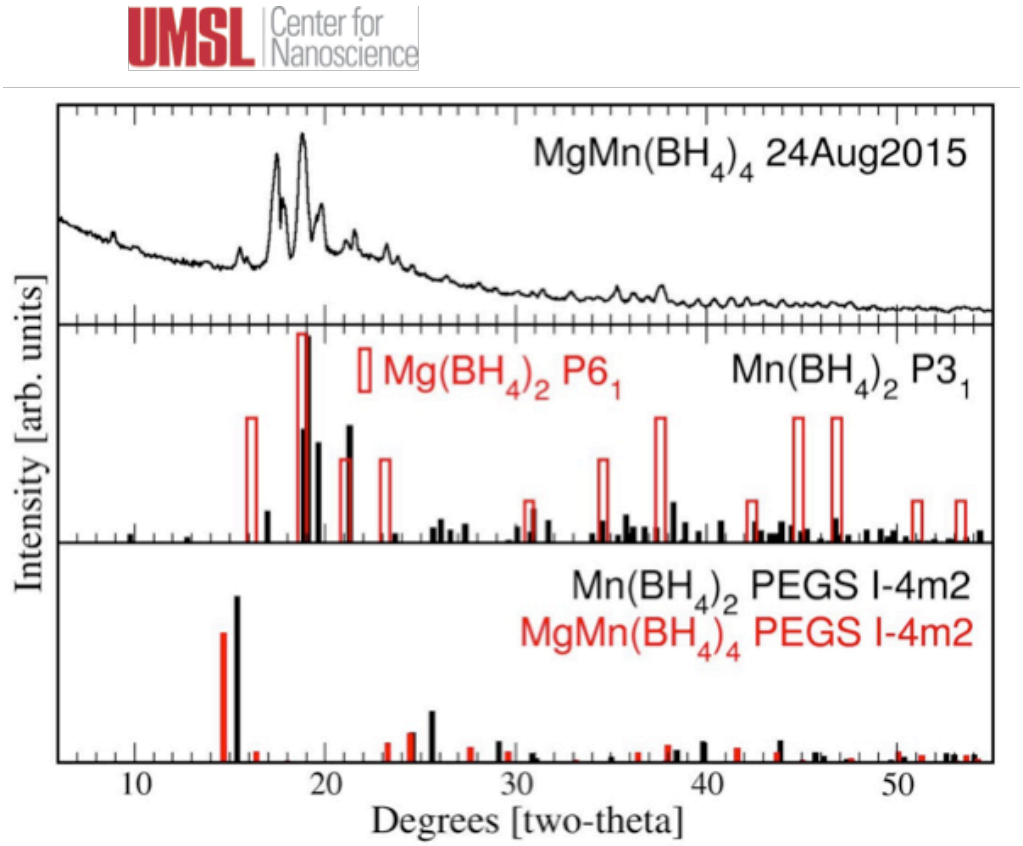

Figure 45. Powder X-ray diffraction of $MgMn(BH_4)_4$ prepared at Sandia (top panel). Calculated diffraction from Filinchuk structure for $Mn(BH_4)_2$ in $P3_1$ (middle panel). Calculated diffraction for $Mn(BH_4)_2$ and $MgMn(BH_4)_4$, both in space group I-4m2.

It also appears that the sample is not simply a phase separated mixture of Mg- and Mn-borohydrides due to the large peaks between 17-18 degrees two-theta, for example. Nonetheless, a PEGS search for $MgMn(BH_4)_4$ results in the lowest energy structure in spacegroup I-4m2, identical to the low energy structure found previously for $Mg(BH_4)_2$.(12) DFT-calculated energies indicate that the lowest energy structures for $Mg(BH_4)_2$ and $Mn(BH_4)_2$ are also in space

group I-4m2. The experimental structure for $MgMn(BH_4)_4$ may contain a very large unit cell as is found in $Mg(BH_4)_2$ in space group $P6_1$ (Figure 45), and would be difficult to find with the PEGS method. All DFT calculations presented below for these structures were for the spacegroup I-4m2. As mentioned above, a PEGS search for $Mn(BH_4)_2$ results in a low energy structure in space group I-4m2 with a lower total energy than in the experimentally observed $P3_1$ (Table 6).

Table 6. Relative energies for $Mn(BH_4)_2$ structures. Total energies were calculated via DFT and include zero point motion.

Compound	Relative Total Energy [kJ/mol]
$Mn(BH_4)_2$ $P3_1$	6.24
$Mn(BH_4)_2$ I-4m2	0

The DFT-calculated energy for the dissociation reaction $MgMn(BH_4)_4 \rightarrow Mg(BH_4)_2 + Mn(BH_4)_2$ at T = 0 K is -20 kJ/mol, indicating that the Mg/Mn mixed borohydride is unstable with respect to decomposition. It may be that the experimentally prepared sample is metastable.

An investigation of the electronic structure of $Mn(BH_4)_2$ and $MgMn(BH_4)_4$ was performed to locate lower energy electronic structures that may affect the calculated thermodynamics. Figure 46 shows the non-spin-polarized total electronic density of states for $Mn(BH_4)_2$ in the I-4m2 structure. Both $Mn(BH_4)_4$ and $MgMn(BH_4)_4$ appear to be metallic.

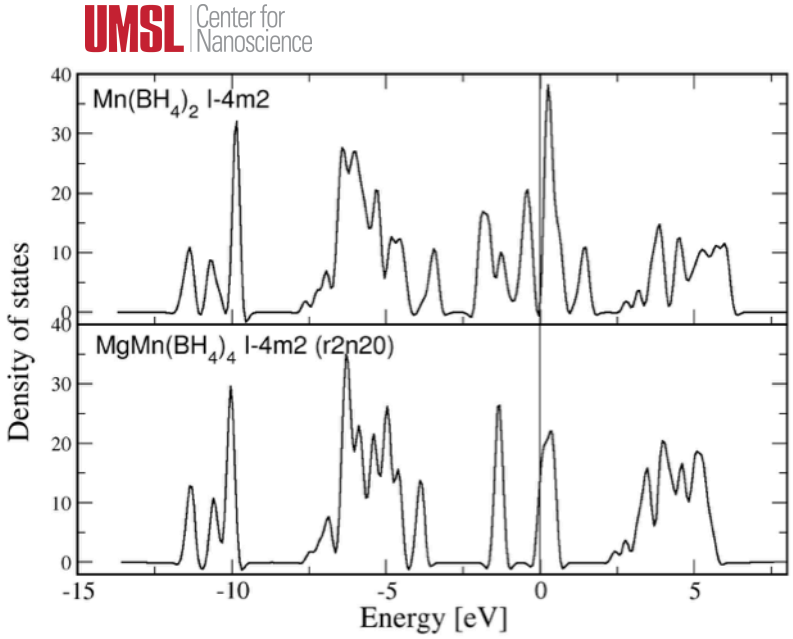

Figure 46. Non-spin-polarized electronic density of states (DOS) for Mn and mixed MgMn borohydrides in space group I-4m2. The Fermi level is shifted to zero and indicated by a vertical line.

The density of states (DOS) and integrated DOS for I-4m2 $Mn(BH_4)_2$ are shown in Figure 47. The integrated electron density around the Mn atoms in this structure gives a total electron count of about 5*e*, while the Mn psueodpotential used in our calculation has a valence of seven, indicating the charge state of Mn in $Mn(BH_4)_2$ is indeed 2+. We find the same result for Mn in $MgMn(BH_4)_4$.

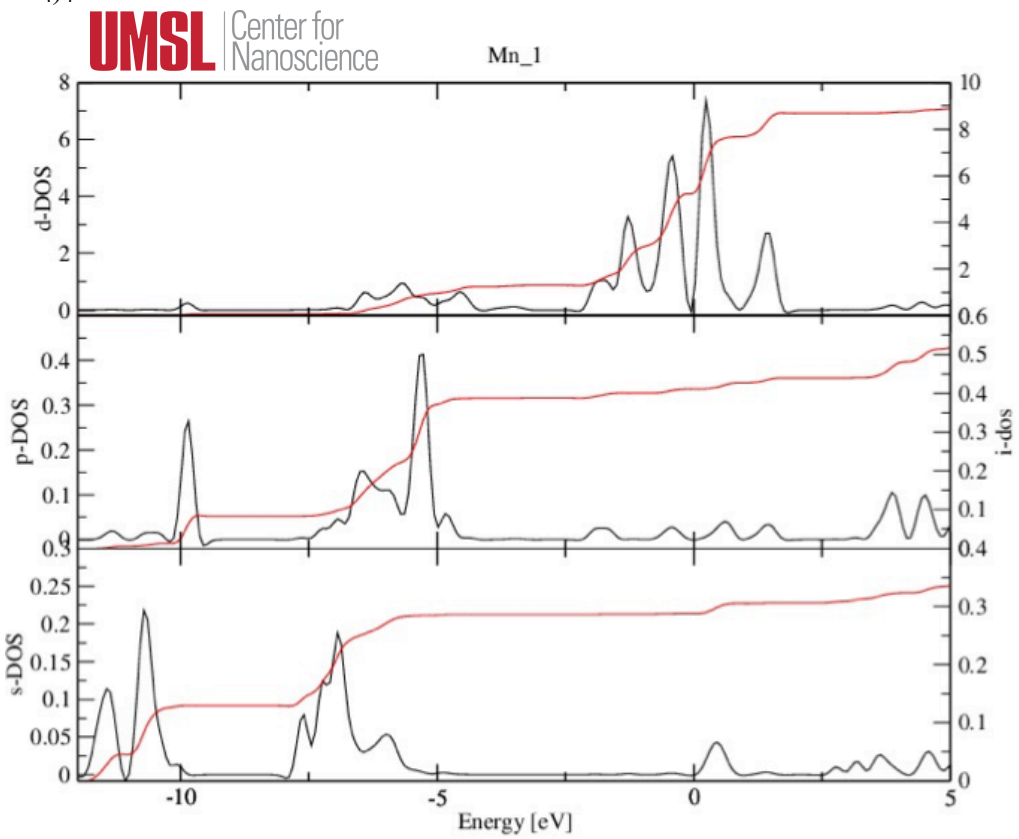

Figure 47. Angular momentum decomposed density of states (DOS) and integrated DOS for Mn in $Mn(BH_4)_2$ in space group I-4m2.

Spin-polarized electronic density of states are shown in Figures 48 and 49. At T = 0K the stable electronic structure is high spin Mn^{2+} with an anti-ferromagnetic spin configuration for both $Mn(BH_4)_2$ and $MgMn(BH_4)_4$. While $Mn(BH_4)_2$ remains metallic, the mixed Mg/Mn borohydride is now predicted to be essentially insulating with a very small gap. These total energy changes do not affect the conclusion that for the structures in symmetry I-4m2, there is no predicted mixing. We conclude two possibilities: Our structure for $MgMn(BH_4)_4$ in I-4m2 yields a much higher energy than the true experimental structure, (Note that our I-4m2 structure is lower in energy than our calculated energy for the structure in the experimentally reported $P3_1$.) or that the mixed $MgMn(BH_4)_4$ compound is metastable.

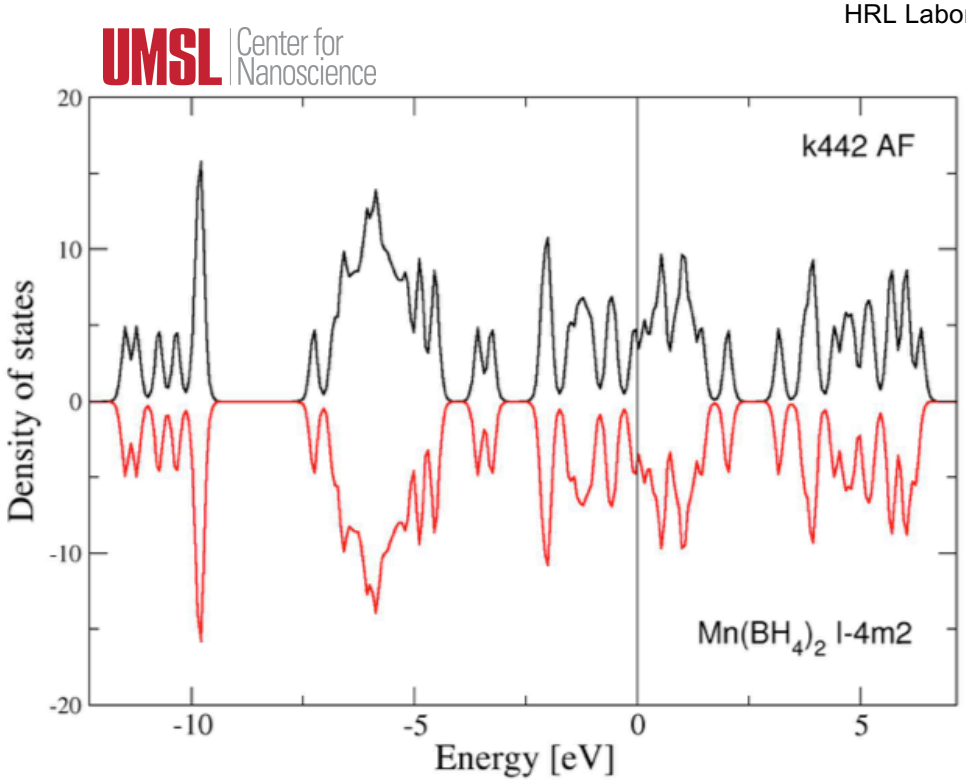

Figure 48. Spin-polarized electronic DOS for $Mn(BH_4)_2$. Spin-up (black) and spin-down (red) populations are identical up to the Fermi energy at 0 eV.

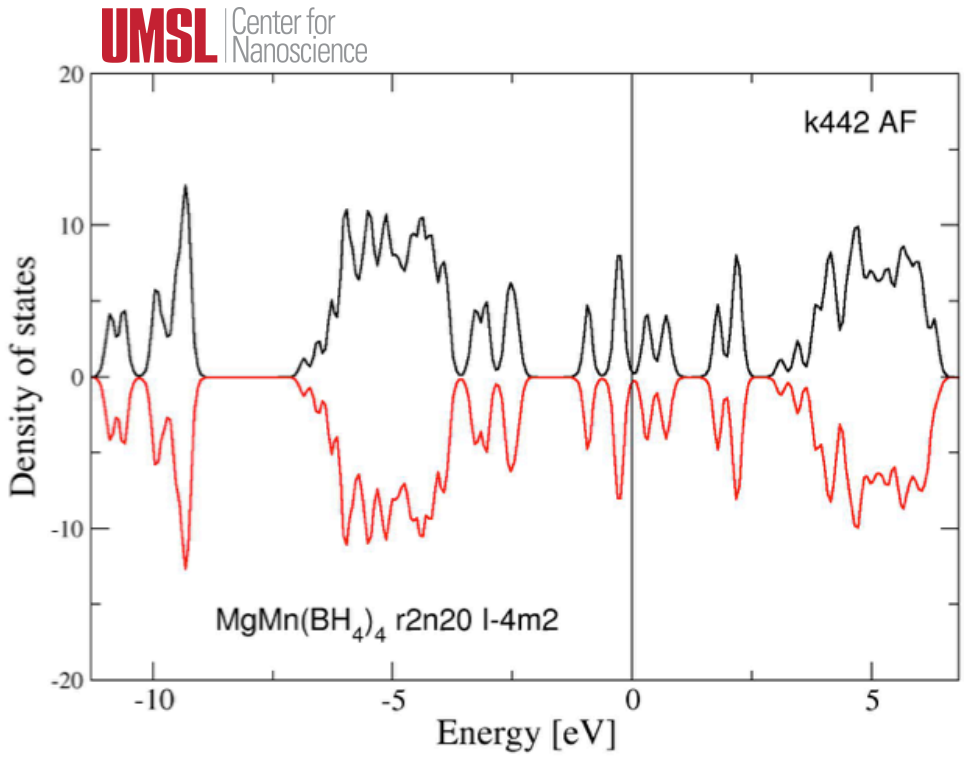

Figure 49. Spin-polarized electronic DOS for $MgMn(BH_4)_4$. Spin-up (black) and spin-down (red) populations are identical up to the Fermi energy at 0 eV.

7.3 Ca-based ternary borides and mixed-metal borohydrides: Initially Mg-based ternary boride and mixed-metal borohydrides were investigated. This work was extended to the formation energy of hypothetical Ca-TM-B ternary borides using the Pbam space group (experimental structures) as prototypes and substituting Ca and TM on the metal sites, with TM = {Sc, Ti, V, Cr, Mn, Fe, Co, Ni}. The results for compounds with composition $CaTMB_6$ and Ca_2TMB_4 are shown in Figure 50 (at T = 0 K including zero point energy). In Figure 50, the reactions involve CaB_6, a very stable Ca-boride phase, and the transition metals forming the ternary boride and a transition metal boride byproduct. Only the early transition metals, Sc, Ti, and V, have clearly exothermic reaction enthalpies. These enthalpies are likely influenced by the stability of the TMB_2 byproduct.

UMSL Center for Nanoscience

Ternary boride	TM	Reactions
$CaTMB_4$	Sc, Ti, V, Cr, Mn	$CaB_6 + 2TM \rightarrow CaTMB_4 + TMB_2$
	Co, Fe, Ni	$CaB_6 + 2TM \rightarrow CaTMB_4 + TMB + B$
Ca_2TMB_6	Sc, Ti, V, Cr, Mn	$2CaB_6 + 4TM \rightarrow Ca_2TMB_6 + 3TMB_2$
	Co, Fe, Ni	$2CaB_6 + 4TM \rightarrow Ca_2TMB_6 + 3TMB + 3B$

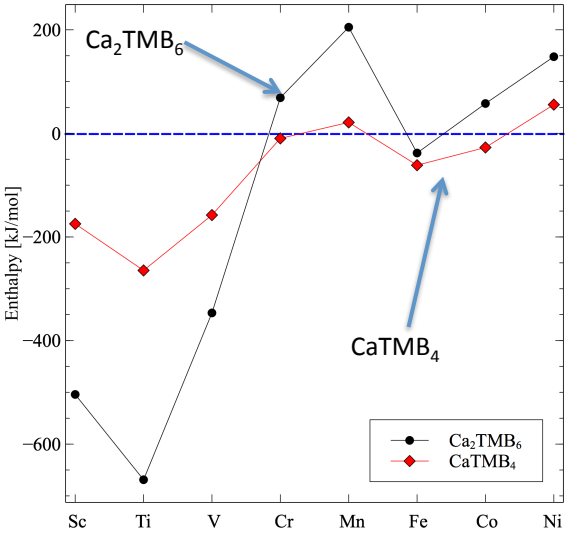

Figure 50. DFT calculations for Ca based ternary borides via reaction of CaB_6 with transition metals (TM).

To synthesize the Ca ternary borides in pure form (no byproducts), reactions of CaB_6 + TM with additional elemental Ca were studied. The results are shown in Figure 51. Favorably exothermic enthalpies are predicted for the $CaTMB_4$ composition for Ti, V, Mn, Fe, and Cr. These results (Figures 50 and 51) address only specific reaction pathways.

For the corresponding hydrogenated mixed-metal borohydrides, PEGS structure calculations were performed for the mixing of $Ca(BH_4)_2$ with $TM(BH_4)_2$. The space group for $Ca(BH_4)_2$ was Fddd and the structure for $TM(BH_4)_2$ was obtained from $Mn(BH_4)_2$ by simply substituting other

TMs for Mn. The results shown in Figure 52 are for T = 0 K including zero point energy. All of the enthalpies are endothermic, indicating that the mixed-metal borohydrides are predicted to be unstable with respect to phase separation into the pure metal compounds. In preliminary calculations, similar results (~60 kJ/mol enthalpies) were obtained for the Mg/Mn mixed-metal borohydrides.

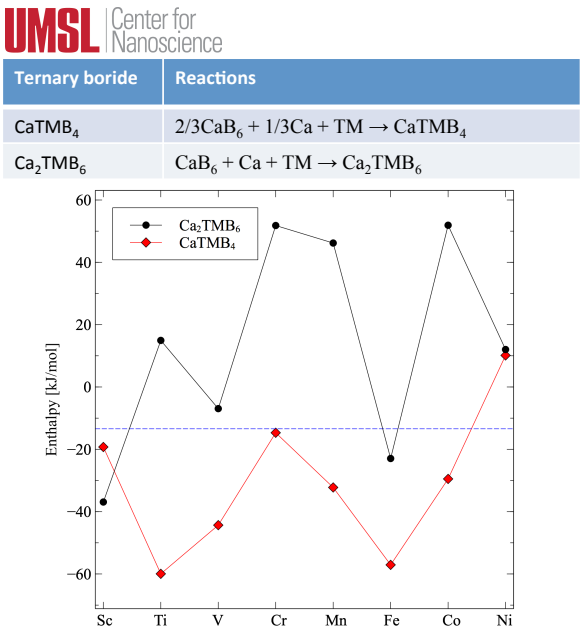

Figure 51. DFT calculations for the direct synthesis Ca based ternary borides.

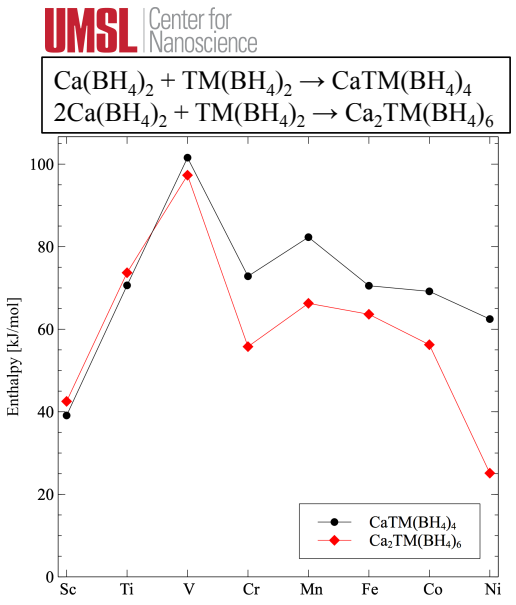

Figure 52. Predicted enthalpies using PEGS structures for formation of Ca based mixed-metal borohydrides.

8. Accomplishment — computational studies of the energetics of lithiated borane hydrogen cycling reactions: Reversible reaction of a borane substrate with lithium hydride to evolve hydrogen and form a lithiated borane has not, to our knowledge, been reported. Thus the energetics of such reactions are not known. To access whether such reactions could have energies suitable for practical hydrogen storage, calculations were performed for Li/H exchange from LiH in a series of small molecular boranes. Initial calculations assumed gas phase boranes for simplicity. Periodic bulk density functional theory calculations of the Li/H exchange energy for solid-state molecular crystals of various small boranes were performed to compare with the first-principles gas-phase calculations. Figure 53 shows the exchange energy, not including zero point energy (ZPE) for borane cluster sizes ranging from B_2H_6 to $B_{18}H_{22}$, for the relatively more stable B_nH_{n+4} clusters. The Inorganic Crystal Structure Database (ICSD) contains structures for $B_{12}H_{16}$ and $B_{18}H_{22}$. For the smaller B_2H_6 and B_5H_9 clusters, the PEGS method was used to generate solid structure candidates using a simple Leonard-Jones potential between the B and H atoms of the clusters. These structure candidates were subsequently relaxed using DFT to obtain total energies. For the small cluster borane structures generated with PEGS, the ZPE was also calculated, and the structures were determined to be dynamically stable. As shown in Figure 53, including ZPE tends to lower the Li/H exchange energy (more exothermic) by about 10 kJ/mol-H_2. It is expected that bulk calculations will differ significantly from gas-phase calculations for small cluster sizes, as is indicated in the figure. As the cluster sizes increase the gas-phase calculations tend toward the bulk. We also note that N-doped boranes in the bulk calculations show increased endothermicity. We expect the bulk calculations to more accurately reflect the experimental results. Given the physical accuracy of the bulk calculations (errors of +/- 10-20 kJ/mol reaction) it is not yet clear whether the exchange reaction studied is endothermic.

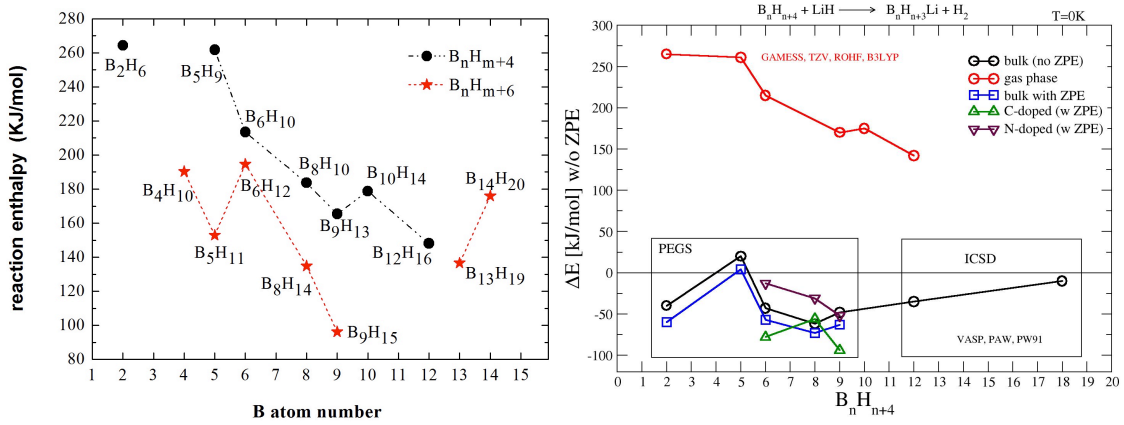

UMSL Center for Nanoscience

Figure 53. Energies for Li/H exchange reactions. Gas-phase single LiH exchange reaction showing BnHn+4 clusters are more stable while BnHn+6 are less stable (left panel). Comparison of first principles gas-phase calculations (top circles, red) with bulk density functional theory calculations (bottom circles, black) including ZPE (squares, blue) all at T = 0 K. As indicated, bulk calculations using PEGS structures for n = 2, 5, 6 and 8 and ICSD structures for n =12 and 18 (right panel).

The gas-phase calculations indicate that the Li/H exchange reaction is too endothermic. We investigated the change in the exchange energy when substituting Cl for H, or O for B on the clusters before Li/H exchange. These substitutions should reduce the electron density on the cluster and make the Li/H exchange less endothermic. Our first-principles calculations support this assumption (Figure 54). We note that the trends in the exchange reaction energies shown in the gas-phase calculations for substitution effects should be in the correct direction (more or less endothermic), even though the bulk calculations should be more representative of our experimental results.

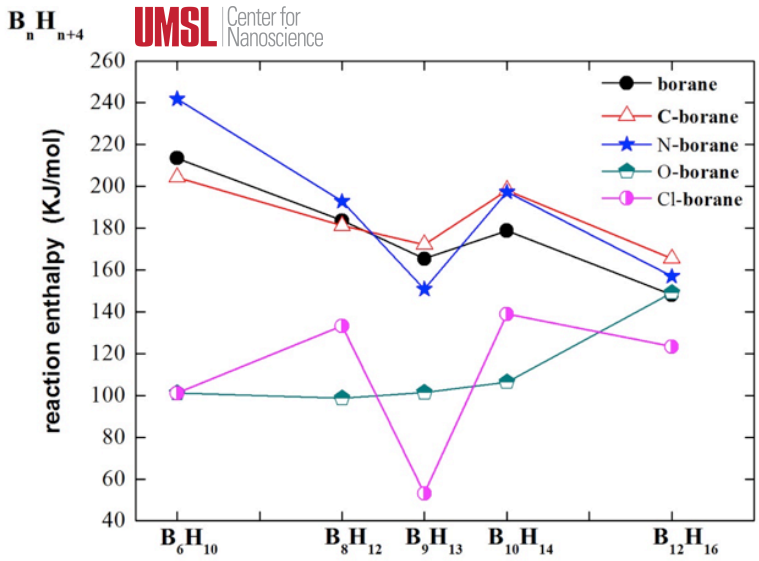

Figure 54. Gas-phase first-principles calculations for the Li/H exchange reaction when substituting electron withdrawing elements Cl, and O, for H and B, respectively. The trend is to make the exchange reaction less endothermic.

Overall, the energetics of these reactions have proven difficult to accurately predict. Initial (computationally simpler) molecular gas phase calculations gave very high endothermic exchange energies (> 100 kJ/mol-H_2), although tellingly there was a steep decline in energy with increasing molecular size. Subsequent, solid state calculations gave exothermic energies that appear to become more endothermic with increasing size. The convergence of these two different approaches suggest exchange energies for boranes, B_nH_x with n>20, of ± 25 kJ/mol-H_2. While this range is very large, the results suggest that a reversible is reaction is feasible. In addition, attention should be focused on polymeric or nanoparticle borane substrates, not molecular species, such as $B_{10}H_{14}$. A similar conclusion was reached experimentally.

9. Summary: The main results from this project may be summarized as follows:

1. Nanocrystalline Mg/Mn ternary metal borides with compositions of $Mg_{0.5}Mn_{0.5}B_2$, $Mg_{0.75}Mn_{0.25}B_2$, and $Mg_{0.9}Mn_{0.1}B_2$ were synthesized directly by high energy mechanical milling of MgB_2 and MnB_2.

2. Computations confirmed the thermodynamic stability of the $Mg_{0.5}Mn_{0.5}B_2$ composition in addition to the same composition for Mg ternary borides with Fe and Co.

3. The $Mg_{0.75}Mn_{0.25}B_2$ composition was predicted to be unstable. Some evidence for this predicted instability was observed by annealing (at 500 °C) the $Mg_{0.75}Mn_{0.25}B_2$ sample synthesized by milling. Thus, the milling likely yielded a metastable composition.

4. The $Mg_{0.75}Mn_{0.25}B_2$ ternary boride could be hydrogenated with a hydrogen uptake of 0.5 to ~1.0 wt% under ~150 bar to 200 bar H_2 at 350 °C to 380 °C. In contrast only trace, at most ~0.05 wt%, hydrogen uptake occurred for pure nanocrystalline MgB_2 under the same conditions.

5. A novel synthetic route using metal alkyls and borane-dimethyl sulfide was developed to synthesize magnesium, manganese, and the mixed-metal magnesium/manganese borohydrides.

6. The magnesium/manganese mixed-metal borohydride $Mg_{0.5}Mn_{0.5}(BH_4)_2$ began to dehydrogenate at 150 °C, which is 100 °C lower than the pure magnesium borohydride. However, on a second cycle the dehydrogenation temperature increased to ~300 °C suggesting that the mixed-metal borohydride did not reform upon rehydrogenation.

7. Computations predicted that the magnesium/manganese mixed-metal borohydride is unstable. This instability may explain the large increase in dehydrogenation temperature observed experimentally. Similar results were obtained form calcium mixed-metal borohydrides.

8. Polymerization of $B_{10}H_{14}$ at 250 °C to 300 °C yielded a polymerized borane with an approximate composition of $BH_{0.7}$.

9. When combined with LiH, polymerized borane appeared to dehydrogenate via a lithiation reaction. Approximately, 0.5 wt% hydrogen could be evolved at 200 °C with <50% capacity retention on a second cycle.

10. Polymerized boranes doped with Al, O, N, and Cl displayed similar behavior to the undoped borane.

11. Computations indicated that large molecular boranes B_nH_x with n>20 had dehydrogenation enthalpies of ±25 kJ/mol-H_2. Differential scanning calorimetry measurements supported an exothermic reaction.

10. Conclusions: The main conclusions from this project are as follows:

1. The ternary metal borides and mixed-metal borohydrides investigated thus far (specifically Mg/TM with TM = Mn, Fe, and Co) are likely not suitable for high capacity hydrogen storage under moderate conditions. Although the $Mg_{0.75}Mn_{0.25}B_2$ ternary boride showed vastly (10x) improved hydrogenation compared to pure MgB_2 and the $Mg_{0.5}Mn_{0.5}(BH_4)_2$ mixed-metal borohydride showed a 100 °C lower dehydrogenation temperature than pure $Mg(BH_4)_2$, the absolute uptake of the ternary boride was small (~1 wt%) and the mixed-metal borohydride was predicted to be unstable and experimentally it did not appear to reform after dehydrogenation.

2. The lithiation reactions studied with boranes and lithium hydrides are unlikely to yield high capacity reversible hydrogen storage materials. Although a lithiation reaction was demonstrated with a polymerized borane substrate, the demonstrated capacity was small (<1 wt%) and the enthalpy of dehydrogenation is likely too low, possibly exothermic. In addition, it appears that the boron atom framework cannot readily be retained. The high propensity for formation of thermodynamically stable $LiBH_4$ during preparation of the borane/lithium hydride composite and/or during hydrogenation irreversibly breaks down the boron atom framework.

11. References:

1. *J. Phys. Chem. C*, **118**, 6084-6089 (2014).
2. *ACS Appl. Mater. Interfaces*, **6**, 8513-8525 (2014).
3. *Mater. Res. Bull.,* **31**, 307-316 (1996).
4. *Chem. Commun.,* **50**, 9761 (2014).
5. *Angew. Chem. Int. Ed.,* **39**, 2349-2353 (2000).
6. *Acta Mater.*, **56**, 949-954 (2008).
7. *Phys. Chem. Chem. Phys.*, **10**, 5859–5862 (2008).
8. *J. Am. Chem. Soc.,* **131**, 230-237 (2009).
9. Newhouse, R. J.; Stavila, V.; Hwang, S.-J.; Klebanoff, L. E.; Zhang, J. Z. "Reversibility and improved hydrogen release of magnesium borohydride", *J. Phys. Chem. C*, **114**, 5224 (2010).
10. Cerny, R; Penin, N.; D'Anna, V.; Hagemann, H.; Durand, E.; Ruzicka, J.; *Acta Met*. **59**, 5171 (2011).
11. Cerny, R.; Penin, N.; Hagemann, H.; Filinchuk, Y.; *J. Phys. Chem. C,* **113***,* 9003–9007 (2009).
12. Ozolins, V.; Majzoub, E.H.; Wolverton, C.; *Phys. Rev. Lett.*, **100**, 135501 (2008).